Efficient non-hydrostatic modelling of 3D wave-induced currents using a subgrid approach

Rijnsdorp, Dirk P.; Smit, Pieter B.; Zijlema, Marcel; Reniers, Ad J.H.M.

DOI
10.1016/j.ocemod.2017.06.012

Publication date
2017

Document Version
Accepted author manuscript

Published in
Ocean Modelling

Efficient non-hydrostatic modelling of 3D wave-induced currents using a subgrid approach

Dirk P. Rijnsdorp[a,b,c,*], Pieter B. Smit[d], Marcel Zijlema[a], Ad J. H. M. Reniers[a]

[a] *Environmental Fluid Mechanics Section, Faculty of Civil Engineering and Geosciences, Delft University of Technology, The Netherlands*
[b] *The UWA Oceans Institute, University of Western Australia, Australia*
[c] *Centre for Offshore Foundation Systems, University of Western Australia, Australia*
[d] *Spoondrift Technologies, Inc., Half Moon Bay, CA, United States*

Abstract

Wave-induced currents are an ubiquitous feature in coastal waters that can spread material over the surf zone and the inner shelf. These currents are typically under resolved in non-hydrostatic wave-flow models due to computational constraints. Specifically, the low vertical resolutions adequate to describe the wave dynamics – and required to feasibly compute at the scales of a field site – are too coarse to account for the relevant details of the three-dimensional (3D) flow field. To describe the relevant dynamics of both wave and currents, while retaining a model framework that can be applied at field scales, we propose a two grid approach to solve the governing equations. With this approach, the vertical accelerations and non-hydrostatic pressures are resolved on a relatively coarse vertical grid (which is sufficient to accurately resolve the wave dynamics), whereas the horizontal velocities and turbulent stresses are resolved on a much finer subgrid (of which the resolution is dictated by the vertical scale of the mean flows). This approach ensures that the discrete pressure Poisson equation – the solution of which dominates the computational effort – is evaluated on the coarse grid scale, thereby greatly improving efficiency, while providing a fine vertical resolution to resolve the vertical variation of the mean flow. This work presents the general methodology, and discusses the numerical implementation in the SWASH wave-flow model. Model predictions are compared with observations of three flume experiments to demonstrate that the subgrid approach captures both the nearshore evolution of the waves, and the wave-induced flows like the undertow profile and longshore current. The accuracy of the subgrid predictions is comparable to fully resolved 3D simulations – but at much reduced computational costs. The findings of this work thereby demonstrate that the subgrid approach has the potential to make 3D non-hydrostatic simulations feasible at the scale of a realistic coastal region.

Keywords: nearshore circulation, wave-induced currents, wave breaking, subgrid, non-hydrostatic modelling, SWASH

*Corresponding author.
Email address: rijnsdorp.dirk@gmail.com (Dirk P. Rijnsdorp)

1. Introduction

Coastal waters are highly dynamic regions where waves become increasingly nonlinear as they approach the shore, break, and eventually dissipate most of their energy in the surf zone. In this nearshore region, processes on the intra wave and wave-group scale excite various flow phenomena. This includes the generation of longshore currents and their instabilities (e.g., Özkan-Haller and Kirby, 1999), rip currents (e.g., MacMahan et al., 2006; Dalrymple et al., 2011), and nearshore eddies (e.g., MacMahan et al., 2004; Clark et al., 2012). Such wave-induced currents are an ubiquitous feature of the coastal region that can spread (floating) material over the surf zone and the inner shelf. Currents can, for example, transport sediments, which is relevant with respect to beach morphology, and disperse pollutants that are harmful for the environment (e.g., oil spills). Furthermore, rip currents can be hazardous with respect to swimmer safety (e.g., McCarroll et al., 2015).

During the last decades, our understanding of the nearshore hydrodynamics has greatly increased by means of laboratory experiments (e.g., Reniers and Battjes, 1997; Haller et al., 2002; Kennedy and Thomas, 2004), field observations (e.g., Ruessink et al., 2001; Feddersen and Guza, 2003; MacMahan et al., 2005), theoretical developments (e.g., Longuet-Higgins and Stewart, 1962, 1964; Craik and Leibovich, 1976; Andrews and Mcintyre, 1978; McWilliams et al., 2004; Mellor, 2016), and by three-dimensional numerical modelling (e.g., Groeneweg and Klopman, 1998; Reniers et al., 2009; Uchiyama et al., 2010; Kumar et al., 2012). The majority of such models assume that the flow dynamics evolve on larger scales (in space and time) compared to the fast wave motion, and that the wave dynamics are locally well represented by small amplitude (linear) wave theory based on geometric optics. These assumptions, which are often reasonable away from the surf zone, allow such models to operate on the scale of the mean flow dynamics, including mean forcing terms due to the wave motion. The dynamics of the wave motion are calculated separately using a phase-averaged wave model. However, in and near the surf zone, where the wave motion becomes strongly skewed and asymmetric due to nonlinear shoaling, and where the waves ultimately break, mean flow dynamics and transport processes are strongly affected by the nonlinear wave dynamics. Consequently, processes like wave breaking, and the influence of skewness and asymmetry on transport are strongly parametrised in these models.

In principle, phase-resolving wave models are available that can be feasibly applied to a realistic field site (say $\sim 10 \times 10$ wave lengths and ~ 1000 wave periods) to resolve these non-linear wave effects. These models, such as Boussinesq(-like) models (e.g., Madsen et al., 1991; Wei et al., 1995; Bonneton et al., 2011) and non-hydrostatic models (e.g., Yamazaki et al., 2009; Zijlema et al., 2011; Ma et al., 2012), all in some form exploit the fact that – in shallow water – the depth over wavelength ratio μ is usually small for the dominant wave motions (i.e., $\mu \ll 1$). Furthermore, they assume that changes in the vertical profile of the wave properties (such as the particle velocities) occur on a vertical scale $L_w\,(= d/\mu)$ that is comparable to the depth d. Because of this slow vertical variability of the wave motion, phase-resolving models have

been able to successfully describe the wave dynamics by either approximating the vertical structure by some appropriate series expansion (Boussinesq models) or by dividing the water column in a few vertical layers (non-hydrostatic models). As long as conservation of momentum is ensured when bores develop, this approach can even be applied to simulate highly nonlinear wave dynamics in the surf zone (e.g., Kennedy et al., 2000; Bradford, 2011; Tissier et al., 2012; Smit et al., 2014). While efficient, the consequence is that the vertical structure of the mean flow is either not resolved (Boussinesq models) or very crudely approximated (non-hydrostatic models). This effectively implies that these models can only resolve the bulk horizontal circulations.

This is not a fundamental restriction of non-hydrostatic models as they can be applied with an arbitrary vertical resolution to resolve the vertical structure of the flow field (e.g., Bradford, 2014; Derakhti et al., 2016a,b). However, a fine vertical resolution is required to resolve the vertical scale of the mean flow (L_c). In the nearshore, L_c can be a fraction of the local depth as flows can develop significant vertical shear. For example, cross-shore circulations can develop with an onshore directed mean flow in the upper part and an offshore directed return flow (or undertow) in the lower part of the water column. Consequently, $L_c/L_w \ll 1$, which implies that the vertical resolution is primarily dictated by the flow scales and not by the wave motion. Resolving the mean flow thus may require $\mathcal{O}(10)$ layers, which becomes impracticable at field scales. For practical applications at these scales, non-hydrostatic models are restricted to at most 1–3 layers (e.g., Rijnsdorp et al., 2015; Gomes et al., 2016; Nicolae Lerma et al., 2017) as the solution of the pressure Poisson equation – which already dominates the computational effort at low resolutions – becomes prohibitively expensive at higher resolutions. This is unfortunate because neither the evolution of the mean dynamics, which behave as shallow water flows, nor the evolution of the wave dynamics, for which 1–3 layers have been found sufficient, require the non-hydrostatic pressure (or vertical accelerations) to be resolved at the vertical scale of the mean flow. Arguably, in intermediate to shallow water a combined wave-flow model needs to resolve the horizontal accelerations on the fine mean flow scale L_c, whereas it can resolve the vertical accelerations and non-hydrostatic pressures on the coarser wave scale L_w.

This observation, and inspired by the work of Van Reeuwijk (2002) and Shi et al. (2015), motivates us to solve the vertical and horizontal momentum balances on essentially separate grids. The vertical balance (and pressure) is evaluated on a coarse grid of which the resolution is dictated by the wave motion, whereas the horizontal balance is solved on a finer grid to account for vertical shear. Given that the solution of the non-hydrostatic pressure field requires most computational effort, the overall model efficiency can be significantly improved by solving the vertical balance and the deviations from hydrostatic pressure at the scales of the wave motions, while maintaining a high vertical resolution to resolve the vertical structure of the wave-induced mean flow field. The hypothesis that the vertical grids on which the velocity and the pressure are calculated can be different for certain flow problems was first presented for linear wave motion by Van Reeuwijk (2002). It has seen little development until Shi et al. (2015) reintroduced the proposition

– which they referred to as the 'Pressure Decimation and Interpolation (PDI)' method. They demonstrated that the non-hydrostatic pressure can be resolved on a separate coarse grid in the context of stratified flow problems.

The main difficulty with this approach is the consistent coupling between the coarse and fine grids. This coupling, which is achieved through the continuity equation and the pressure interpolation, influences whether or not the method conserves mass and momentum on all grid scales (e.g., the PDI method only conserves mass on the coarse grid, but not on the fine grid). In turn, this influences the dispersive properties of the short waves (as will be shown in this paper). As our primary interest is to efficiently resolve both the waves and the (wave-driven) sheared flows in the coastal zone, we will present a derivation of – what we call – a subgrid approach and the coupling between the grids that is tailored towards this application. Our approach differs from Shi et al. (2015) in how the pressure is interpolated, and that only the horizontal velocities are dynamically resolved on the fine grid. In our derivation it is most natural to view the resulting model as an extension of an existing coarse grid model with a subgrid model to account for vertical shear (and not as a reduction of a fine grid model). For that reason, we refer to our methodology as a subgrid approach.

In Section 2, we present the derivation of the subgrid approach and discuss its numerical implementation in the SWASH model[1] (Zijlema et al., 2011). This is followed by a linear analysis of the model equations to motivate our choice for the pressure interpolation (Section 3). To assess the performance of the method, we validated the model for three test cases that consider the evolution of the wave and flow field in a coastal environment (Section 4). Finally, we discuss and summarise our findings in Section 5 and 6, respectively.

2. Numerical Methodology

The starting point of this work is the Reynolds-averaged Navier-Stokes (RANS) equations for an incompressible fluid of constant density. We consider a fluid that is bounded in the vertical by the bottom $z = -d(x, y)$ and the free surface $z = \zeta(x, y, t)$; where t is time, $\langle x, y, z \rangle$ are the Cartesian coordinates, and the still water level is located at $z = 0$. In this framework, the governing equations read,

[1]The SWASH code, including the subgrid approach, can be used freely under the GNU GPL license (`http://swash.sourceforge.net`).

$$\frac{\partial u}{\partial x}+\frac{\partial v}{\partial y}+\frac{\partial w}{\partial z}=0, \tag{1}$$

$$\frac{\partial u}{\partial t}+\frac{\partial uu}{\partial x}+\frac{\partial uv}{\partial y}+\frac{\partial uw}{\partial z}+g\frac{\partial \zeta}{\partial x}+\frac{\partial q}{\partial x}=\frac{\partial \tau_{xx}}{\partial x}+\frac{\partial \tau_{xy}}{\partial y}+\frac{\partial \tau_{xz}}{\partial z}, \tag{2}$$

$$\frac{\partial v}{\partial t}+\frac{\partial vu}{\partial x}+\frac{\partial vv}{\partial y}+\frac{\partial vw}{\partial z}+g\frac{\partial \zeta}{\partial y}+\frac{\partial q}{\partial y}=\frac{\partial \tau_{yx}}{\partial x}+\frac{\partial \tau_{yy}}{\partial y}+\frac{\partial \tau_{yz}}{\partial z}, \tag{3}$$

$$\frac{\partial w}{\partial t}+\frac{\partial wu}{\partial x}+\frac{\partial wv}{\partial y}+\frac{\partial ww}{\partial z}+\frac{\partial q}{\partial z}=\frac{\partial \tau_{zx}}{\partial x}+\frac{\partial \tau_{zy}}{\partial y}+\frac{\partial \tau_{zz}}{\partial z}, \tag{4}$$

where u is the velocity component in x-direction, v is the velocity component in y-direction, w is the velocity component in z-direction, g is the gravitational acceleration, and $\tau_{\alpha\beta}$ represent the turbulent stresses (where α or β denote the coordinates). The turbulent stresses are estimated using an eddy viscosity approximation (Appendix A). In this set of equations, the total pressure is decomposed in the hydrostatic $\rho g\,(\zeta - z)$ and non-hydrostatic component ρq, with q the normalised non-hydrostatic pressure.

Assuming that the vertical fluid boundaries are a single valued function of the horizontal coordinate, the following kinematic conditions apply at the free surface and (impenetrable and immobile) bottom,

$$w|_{z=\zeta}=\frac{\partial \zeta}{\partial t}+u\frac{\partial \zeta}{\partial x}+v\frac{\partial \zeta}{\partial y}, \tag{5}$$

$$w|_{z=-d}=-u\frac{\partial d}{\partial x}-v\frac{\partial d}{\partial y}. \tag{6}$$

Integrating the local continuity equation, Eq. (1), over the water column and applying the relevant kinematic boundary conditions yields a global continuity equation that describes the temporal evolution of the free surface,

$$\frac{\partial \zeta}{\partial t}+\frac{\partial}{\partial x}\int_{-d}^{\zeta} u\mathrm{d}z+\frac{\partial}{\partial y}\int_{-d}^{\zeta} v\mathrm{d}z=0. \tag{7}$$

This global continuity equation provides a convenient form to ensure that the numerical approximations are mass conservative.

To get a unique solution, boundary conditions are required at all boundaries of the physical domain (i.e., the free surface, the bottom, and the horizontal boundaries). Neglecting the viscous stresses and the influence of surface tension, and assuming that the atmospheric pressure is constant (and equal to zero for convenience), the non-hydrostatic pressure is set to zero at the free surface $q|_{z=\zeta}=0$ (e.g., Stelling and Zijlema, 2003). At the bottom, the vertical velocity is computed following Eq. (6). Furthermore, two tangential stresses are specified at the bottom, which are estimated using the law of the wall for a typical roughness height d_r (Launder and Spalding, 1974). Using suitable horizontal boundary conditions (typically based on a prescribed form of the horizontal velocity), and a turbulence closure model to compute the eddy viscosities (see Appendix A), this set of equations forms the basis of the model.

In essence, the assumption of a single-valued surface sets non-hydrostatic models apart from more complete descriptions such as volume of fluid (VOF) models (e.g., Lin and Liu, 1998). The single-valued surface does not allow non-hydrostatic models to capture the overturning of the surface, nor the generation of an air-water mixture when waves are breaking. This assumption implies that the model does not directly represent the transformation of organized wave energy into turbulence during the breaking of waves. Instead, breaking waves are represented as shock waves and the breaking process is considered analogous with a hydraulic bore. Its energy dissipation is obtained by ensuring that the weak form of the equations conserve momentum. We stress that this only accounts for the bulk dissipation. Furthermore, the energy is lost from the system rather than inserted into the turbulent kinetic energy budget. Although the enhanced horizontal and vertical shear in the bore region does lead to an increased production of turbulent kinetic energy, this is likely an insufficient proxy for the turbulence generated by the breaking waves through, for example, the development of an air-water mixture. The turbulence injected in the water column by the breaking process, and the influence thereof on the mean flow is thus not fully accounted for and arguably requires explicit parametrisation. This is beyond the scope of the present work and is not taken into account.

Recognizing the existence of different vertical scales for the wave and mean flow dynamics, we intend to solve these equations on two different grids; a coarse grid that is assumed sufficiently accurate to describe the wave dynamics, and a fine subgrid that is able to represent the vertical shear of the mean flow. In the following, we present the balances on the coarse and fine vertical grid, and the coupling between the two. To keep the presentation focussed and concise, we retain a continuous description in space and time, and focus on the aspects of the subgrid approach. Furthermore, we will present the subgrid implementation for a two-dimensional vertical plane (i.e., ignoring the $y-$dimension). The extension to three dimensions is relatively straightforward, does not alter the numerical approach, and will therefore not be detailed here.

2.1. Coarse grid balance

The coarse grid divides the water column in a fixed number P of terrain-following layers (Fig. 1), with a spatially varying layer thickness $H_p \left(= \frac{d+\eta}{P}\right)$. A staggered arrangement is used to position the variables on the grid. The horizontal velocities U are located at the centre of the horizontal cell faces (Z_p), and the vertical velocities W and non-hydrostatic pressures Q are located at the centre of the vertical cell faces ($Z_{p^\pm}$). Each coarse layer p is subsequently divided into a constant number N of subgrid layers k ($N = K/P$, where K is the total number of subgrid layers). Similar to the coarse grid variables, the subgrid variables are arranged using a staggered arrangement. In the following, lower-case symbols correspond to continuous variables (e.g., u), capital symbols with subscripts correspond to a coarse grid variable (e.g., U_p) and lower-case symbols with subscripts correspond to a subgrid variable (e.g., $u_{p,k}$).

The governing equation for the free surface is given by the global continuity equation. Since the depth integrated discharge is the sum of the layer discharges (which are by definition H_pU_p) the global continuity

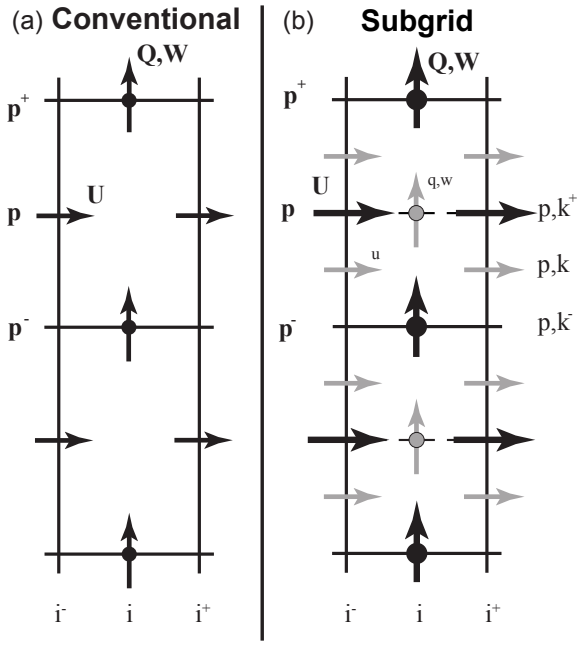

Figure 1: Staggered variable arrangement on the numerical grid. The left panel shows the arrangement according to the conventional SWASH model, and the right panel shows the arrangement used in the case of the subgrid method. In (b), the grey symbols correspond to the variables on the finer velocity grid, and the black symbols correspond to the variables on the coarse pressure grid. Note that the fine and coarse grid non-hydrostatic pressures and vertical velocities overlap at the vertical faces (p^+ and p^-) of a pressure layer.

equation is evaluated as,

$$\frac{\partial \zeta}{\partial t} + \sum_{p=1}^{P} \frac{\partial H_p U_p}{\partial x} = 0. \tag{8}$$

Vertically integrating the local continuity equation over a layer p, and making use of the Leibniz integration rule, results in the following coarse grid local continuity equation,

$$\frac{\partial H_p U_p}{\partial x} + W_{p^+} - W_{p^-} - \overline{U}_{p^+} \frac{\partial Z_{p^+}}{\partial x} + \overline{U}_{p^-} \frac{\partial Z_{p^-}}{\partial x} = 0, \tag{9}$$

where the horizontal velocity at the interfaces $\overline{U}_{p^\pm}$ are estimated from the U_p values by means of linear interpolation.

The time evolution of $H_{p^+} W_{p^+}$ is dictated by the vertical momentum balance, Eq. (4), which after vertical integration over the interval $Z_p \leq z \leq Z_{p+1}$ reads,

$$\frac{\partial H_{p^+} W_{p^+}}{\partial t} + \frac{\partial}{\partial x}\left(H_{p^+} \left\langle uw \right\rangle_{Z_{p^+}} \right) + \hat{W}_{p+1} \overline{\Omega}_{p+1} - \hat{W}_p \overline{\Omega}_p = -H_{p^+} \left\langle \frac{\partial q}{\partial z} \right\rangle_{Z_{p^+}}, \tag{10}$$

where we neglected the effect of turbulent stresses. Here, the angled brackets indicate averaging over a coarse $w-$velocity layer,

$$\langle \ldots \rangle_{Z_p^+} = \frac{1}{Z_{p+1} - Z_p} \int_{Z_p}^{Z_{p+1}} \ldots \, \mathrm{d}z,$$

and $\overline{\Omega}_p$ is the relative vertical advective velocity that is interpolated from the relative vertical velocities at the layer interfaces Ω_{p^+}, which are formally defined as,

$$\Omega_{p^+} = W_{p^+} - \frac{\partial Z_{p^+}}{\partial t} - \overline{U}_{p^+} \frac{\partial Z_{p^+}}{\partial x}.$$

The transported vertical momentum $\hat{W}_p$ is obtained using a suitable (flux limited) interpolation from W_{p^+}, and we set $\langle uw \rangle_{Z_{p^+}} \approx \overline{U}_{p^+} W_{p^+}$ (which is consistent with the assumption that W changes slowly within a pressure layer). Because of its favorable dispersive properties for the barotropic modes (e.g., Stelling and Zijlema, 2003), the layer averaged non-hydrostatic pressure gradient $\left\langle \frac{\partial q}{\partial z} \right\rangle_{Z_p}$ is approximated using the Hermetian relation,

$$\left\langle \frac{\partial q}{\partial z} \right\rangle_{Z_{p^+}} + \left\langle \frac{\partial q}{\partial z} \right\rangle_{Z_{p^-}} = 2 \frac{Q_{p^+} - Q_{p^-}}{H_p}.$$

Lastly, the time evolution of $H_p U_p$ follows from the coarse layer integrated horizontal momentum balance, Eq. (2),

$$\frac{\partial H_p U_p}{\partial t} + H_p \left\langle \frac{\partial uu}{\partial x} + \frac{\partial uw}{\partial z} \right\rangle_{Z_p} = -g H_p \frac{\partial \zeta}{\partial x} + H_p \left\langle \frac{\partial \tau_{xx}}{\partial x} + \frac{\partial \tau_{xz}}{\partial z} - \frac{\partial q}{\partial x} \right\rangle_{Z_p} + U \frac{\partial z}{\partial t} \Bigg|_{Z_{p^-}}^{Z_{p^+}} \tag{11}$$

in which $\langle \ldots \rangle_{Z_p}$ indicate averaging over a coarse $u-$velocity layer with lower bound Z_{p^-} and upper bound Z_{p^+}.

Up to this point, our procedure closely follows the original SWASH model (e.g., Zijlema and Stelling, 2008; Zijlema et al., 2011). In fact, if the as of yet unspecified (layer averaged) forcing terms related to advection, pressure, turbulent stresses, and the moving grid are expressed in terms of the coarse grid variables, we effectively regain the conventional set of equations that is approximated in SWASH. However, in that case, a large number of coarse pressure layers is required to resolve the vertical variability of the flow that is driven by the divergence of the stress in the horizontal balance.

2.2. Subgrid balance

Instead of closing the coarse grid equations directly, each pressure layer is divided into N subgrid layers. The aim of this subgrid approach is to dynamically account for the flow that is driven by the divergence of the stresses in the horizontal balance, even if these are not resolved on the coarse grid. For this purpose, we integrate Eq. (2) over a subgrid layer k to obtain the time evolution of the horizontal subgrid discharges,

$$\frac{\partial h_{p,k}u_{p,k}}{\partial t} + \frac{\partial h_{p,k}u_{p,k}^2}{\partial x} + \hat{u}_{p,k^+}\omega_{p,k^+} - \hat{u}_{p,k^-}\omega_{p,k^-} = -gh_{p,k}\frac{\partial \zeta}{\partial x} - h_{p,k}\left\langle \frac{\partial q}{\partial x} \right\rangle_{z_{p,k}} + h_{p,k}\left\langle \frac{\partial \tau_{xx}}{\partial x} + \frac{\partial \tau_{xz}}{\partial z} \right\rangle_{z_{p,k}}, \tag{12}$$

where subscript p,k indicates the subgrid layer ($k = 1 \ldots N$) in coarse layer p, and in which we introduced the approximation $\left\langle u^2 \right\rangle_{z_{p,k}} \approx u_{p,k}^2$. The angled brackets indicate averaging over a subgrid $u-$velocity layer,

$$\langle \ldots \rangle_{z_{p,k}} = \frac{1}{z_{p,k^+} - z_{p,k^-}} \int_{z_{p,k^-}}^{z_{p,k^+}} \ldots \, \mathrm{d}z.$$

The transported horizontal momentum $\hat{u}_{p,k^\pm}$ is obtained from a suitable (flux limited) interpolation from $u_{p,k}$, and ω_{p,k^+} is the subgrid relative velocity (to be defined below). The turbulent stress terms are approximated on the fine grid,

$$\left\langle \frac{\partial \tau_{xx}}{\partial x} + \frac{\partial \tau_{xz}}{\partial z} \right\rangle_{z_{p,k}} \approx \frac{1}{h_{p,k}} \left[\frac{\partial h_{p,k}\tau_{xx,p,k}}{\partial x} - \overline{\tau}_{xx,p,k^+}\frac{\partial z_{p,k^+}}{\partial x} + \overline{\tau}_{xx,p,k^-}\frac{\partial z_{p,k^-}}{\partial x} + \tau_{xz,p,k^+} - \tau_{xz,p,k^-} \right],$$

with

$$\tau_{xx,p,k} = 2\nu_x \frac{\partial u_{p,k}}{\partial x}, \qquad \tau_{xz,p,k^+} = \nu_z \left[\frac{u_{p,k+1} - u_{p,k}}{h_{p,k^+}} + \frac{\partial w_{p,k^+}}{\partial x} \right], \qquad \overline{\tau}_{xx,p,k^+} = \frac{\tau_{xx,p,k} + \tau_{xx,p,k+1}}{2}.$$

The non-hydrostatic pressure gradient is evaluated based on subgrid pressures that are interpolated from the coarse grid pressures (Q_p). In the literature (Van Reeuwijk, 2002; Shi et al., 2015), different spline based interpolation techniques have been proposed to provide a smooth and accurate interpolation. In contrast with these studies, we use linear interpolation to approximate the subgrid non-hydrostatic pressures – this choice is motivated in Section 3. Here, we only wish to highlight that it is consistent with the assumption of slow intra-layer variations in the non-hydrostatic pressure. Consequently, the non-hydrostatic pressure at the subgrid layer interface p,k^+ is computed as,

$$\tilde{q}_{p,k^+} = Q_{p^-} + (z_{p,k^+} - Z_{p^-})\frac{Q_{p^+} - Q_{p^-}}{H_p}.$$

The non-hydrostatic pressure gradient is subsequently evaluated as,

$$\left\langle \frac{\partial q}{\partial x} \right\rangle_{z_{p,k}} = \frac{1}{h_{p,k}} \left[\frac{\partial}{\partial x} \frac{h_{p,k}(\tilde{q}_{p,k^+} + \tilde{q}_{p,k^-})}{2} - \tilde{q}_{p,k^+}\frac{\partial z_{p,k^+}}{\partial x} + \tilde{q}_{p,k^-}\frac{\partial z_{p,k^-}}{\partial x} \right].$$

To couple the coarse grid with the subgrid description, the coarse layer discharges in Eq. (8–9) are defined as the sum of the subgrid layer discharges,

$$H_p U_p = \sum_{k=1}^{N} h_{p,k}u_{p,k}. \tag{13}$$

Furthermore, we need to define the subgrid vertical velocity $w_{p,k^\pm}$ to close the set of equations. This subgrid velocity appears in the turbulent stress terms, and in the definition of the subgrid relative vertical velocity,

$$\omega_{p,k^+} = w_{p,k^+} - \frac{\partial z_{p,k^+}}{\partial t} - \overline{u}_{p,k^+}\frac{\partial z_{p,k^+}}{\partial x}. \tag{14}$$

Because vertical accelerations are assumed to be well described on the coarse grid, we do not introduce a dynamical equation for $w_{p,k^\pm}$. Instead, we compute it based on the subgrid integrated local continuity equation,

$$\frac{\partial h_{p,k}u_{p,k}}{\partial x} + w_{p,k^+} - w_{p,k^-} - \overline{u}_{p,k^+}\frac{\partial z_{p,k^+}}{\partial x} + \overline{u}_{p,k^-}\frac{\partial z_{p,k^-}}{\partial x} = 0, \tag{15}$$

where $\overline{u}_{p,k^+}$ are the horizontal velocities at the layer interfaces. In this manner, the subgrid vertical velocities inside a pressure layer are computed following,

$$w_{p,k^+} = W_{p^-} - \sum_{m=1}^{k}\frac{\partial h_{p,m}u_{p,m}}{\partial x} + \overline{u}_{p,k^+}\frac{\partial z_{p,k^+}}{\partial x}. \tag{16}$$

At the interfaces where the coarse and subgrid vertical velocities coincide (i.e., when $k = 1 \vee k = N$), the subgrid vertical velocities are set to be equal to the respective coarse grid vertical velocities. This also implies that the interpolated $\overline{u}_{p,k^+}$ velocity in Eq. (16) has to match the interpolated velocity on the coarse grid $\overline{U}_{p^+}$ in Eq. (9). Previously, we made the tentative choice to interpolate $\overline{U}_{p^+}$ from the coarse grid velocities, but in principal the interface velocities could be obtained from either the fine or the coarse grid velocities. That said, for steep waves (or bottom gradients) the interface terms strongly contribute to the coarse-grid continuity equation and through it influence the non-hydrostatic distribution. In this case, a strong coupling between the coarse grid velocities and pressures is preferred. For this reason, we interpolate $\overline{U}_{p^+}$ from U_p, and we take $\overline{u}_{p,k^+} = \overline{U}_{p^+}$ in Eq. (14-16) when $k = 1 \vee k = N$.

This completes the description of the subgrid approach, in which we approximate Eq. (1–7) with the semi-discrete set of Eq. (8–10) for $p = 1 \ldots P$, and Eq. (12) for $k = 1 \ldots N$ in each pressure layer, combined with the closure relations Eq. (13) and (16), coupled to a standard $k - \epsilon$ turbulence closure model that is solved using the fine grid velocities. While similar in spirit, the present approach differs from the method advocated by Shi et al. (2015) in two significant ways: a) we use linear interpolation for the pressure profile instead of cubic spline interpolation for reasons expanded upon in Section 3, and b) we do not solve dynamical equations for the subgrid vertical velocities, but instead retrieve $w_{p,k}$ from the subgrid local continuity equation. The latter ensures that incompressibility is ensured on both the subgrid and the coarse grid.

2.3. Numerical implementation

To highlight the essential steps of the subgrid framework, we retained a continuous description in horizontal space and time. However, to obtain a complete numerical model we need to replace the continuous

descriptions with discrete approximations. To this end, we closely follow the methodology of the original SWASH model (Zijlema and Stelling, 2005, 2008; Zijlema et al., 2011). This not only allows us to implement the subgrid approach in the existing and well verified SWASH model, but this also allows us to directly compare the model with and without subgrid approximations. Because the subgrid approach introduced previously does not alter the methodology of SWASH fundamentally, and because the time and space discretisation are not fundamental to the approach advocated here, we will only describe the essential aspects here.

The governing equations are discretised on a curvilinear spatial grid. The flow variables are positioned on the grid using a staggered variable arrangement, in which pressures and vertical velocities are co-located horizontally, and staggered with regards to the horizontal velocities (see Fig. 1). Consequently, horizontal gradients of the surface, discharge and non-hydrostatic pressure can straightforwardly be approximated with central differences. Time-integration of the coupling between hydrostatic pressure and horizontal velocities is performed with the explicit leapfrog scheme, so that horizontal velocities and surface elevation are staggered in space and time (following Hansen, 1956). Horizontal nonlinear advective terms are approximated with a second order flux-limited explicit McCormack scheme (in space and time) using the approximations proposed in Stelling and Duinmeijer (2003) to ensure momentum conservation (and thus the ability to handle shocks) within the context of a staggered framework. Further, to avoid stringent stability conditions for thin water layers, implicit time integration is used to account for the vertical exchange of momentum.

If we neglect the non-hydrostatic pressures, the resultant model is essentially a second-order accurate (in space and time) layered shallow-water model. To incorporate the non-hydrostatic pressure, which is implicitly determined by the coupling between the local continuity equation and the pressure, we use a second-order accurate fractional step method, known as the pressure correction technique (van Kan, 1986), to solve the set of discretised equations. This method constructs a discrete analogue of the pressure Poisson equation by substituting the discrete form of the momentum equations into the discrete continuity equation. For a model with M horizontal grid points and P pressure layers this results in a large but sparse linear system of MP equations with MP unknowns which is subsequently solved using an iterative method to obtain the non-hydrostatic pressure (see Zijlema and Stelling, 2005, 2008; Zijlema et al., 2011, for further details).

Since its inception, the SWASH model has been successfully used to study various wave dynamics in coastal regions. For example, the model has been used to simulate the nearshore evolution of short waves (e.g., Smit et al., 2014; Buckley et al., 2014; Gomes et al., 2016), including their depth-induced breaking and associated bulk dissipation (e.g., Smit et al., 2013), the evolution of infragravity waves in coastal regions (e.g., Rijnsdorp et al., 2014, 2015; De Bakker et al., 2016), and runup oscillations at the beach (e.g., Ruju et al., 2014; Nicolae Lerma et al., 2017). To date, most studies focussed on laboratory scales due to computational constraints. However, with the ever increasing computational capabilities, several recent

studies have demonstrated that field scale applications are now within the reach of state-of-the-art multi-core machines (Rijnsdorp et al., 2015; Gomes et al., 2016; Nicolae Lerma et al., 2017).

3. Linear analysis subgrid method

The basic assumption of the subgrid approach is that the leading order pressure distribution $q(z)$ can be parametrised with a finite number of discrete pressure points q_p located at the interfaces of the coarse pressure grid, so that pressure-layer profile in the subgrid layers is interpolated from the coarse grid values. In the previous section we tentatively used a linear distribution for the intra-layer pressure, and here we will expand on the reasons for that choice.

Following Shi et al. (2015) we describe the pressure by a spline curve $\tilde{q}(z)$ that in each coarse pressure layer takes the form of a polynomial of order N_p,

$$\tilde{q}_p^{N_p} = \sum_{n=0}^{N_p} \alpha_{p,n}(z - Z_p)^{N_p}, \tag{17}$$

where, to avoid strongly oscillatory behaviour, generally $N_p \leq 3$. To uniquely specify the coefficients in terms of the discrete pressures (i.e., $\alpha_{p,n} = \sum_{m=0}^{P} \beta_{p,n,m} q_m$), we need $P(N_p + 1)$ restrictions. These follow from enforcing that the first $N_p - 1$ derivatives are continuous at the coarse-grid layer-interfaces, coupled with (for $P > 1$) the conditions at the surface and bottom (Shi et al., 2015),

$$\partial_z \tilde{q}|_{z=-d} = 0, \qquad \partial_z^2 \tilde{q}|_{z=\zeta} = 0. \tag{18}$$

Although such splines are smooth functions, they may (except for $N_p = 1$) introduce new maxima in the intra-layer pressures[2].

In order to analyze the linear properties, we assume that the dominant errors are associated with the vertical discretisation and therefore consider a semi-discrete description in which the horizontal coordinate and time remain continuous (e.g., following Cui et al., 2012; Bai and Cheung, 2013; Smit et al., 2014). Further, we will assume monochromatic progressive wave motion (propagating in the positive x direction) in a domain of constant depth such that the ratio between the amplitude and a typical vertical scale (ϵ) is small.

[2]Monotone behaviour can be achieved for $N_p = 3$, if the derivatives are allowed to be discontinuous at the interface and instead we demand that $\partial_z \tilde{q}^{N_p} = 0$ at the layer interfaces. This is analogous to Van Reeuwijk (2002), who constructed monotone profiles for the pressure gradient (and therefore used a spline with $N_p = 4$ and enforced $\partial_z^2 \tilde{q}^{N_p} = 0$ at the interfaces). However, $\partial_z \tilde{q}^{N_p} = 0$ implies that vertical accelerations vanish at the cell interfaces and therefore will not be considered here.

The horizontal momentum equations then represent a leading order balance between pressure gradients (hydrostatic and non-hydrostatic) and the local accelerations. Substituting the parametrisation of the pressure, integrating over each individual subgrid layer (neglecting the layer motion, consistent with the assumption of $O(\epsilon)$ dynamics), and summing over all velocity layers within a coarse pressure layer we find that,

$$H_p \left[\frac{\partial U_p}{\partial t} + g \frac{\partial \zeta}{\partial x} \right] = -\frac{\partial}{\partial x} \int_{Z_{p^-}}^{Z_{p^+}} \tilde{q}_p \, \mathrm{d}z = -\sum_{n=0}^{N_p} \sum_{m=0}^{K/P} \frac{\beta_{n,p,m}}{n+1} H_p^{n+1} \frac{\partial q_m}{\partial x}. \tag{19}$$

Consequently, the coarse grid velocity in a layer p depends on a weighted sum of the pressure gradients at the subgrid layers. For $N = 1$ (linear interpolation), the coarse grid velocity at p only depends on the gradients of the local pressure at $Z_{p^\pm}$. In contrast, for $N > 1$ the grid velocity potentially depends on all the pressure gradients in the water column.

Further, by integrating over a coarse layer (and using the Hermetian approximation for the vertical pressure gradient) we obtain at $O(\epsilon)$ the semi-discrete vertical momentum balance and continuity equation,

$$\frac{\partial W_p}{\partial t} + \frac{\partial W_{p-1}}{\partial t} + \frac{q_p - q_{p-1}}{H_p} = 0, \tag{20}$$

$$\frac{\partial U_p}{\partial x} + \frac{W_{p-1} - W_p}{H_p} = 0. \tag{21}$$

Coupled with the boundary conditions $W_P = \frac{\partial \zeta}{\partial t}$, $W_0 = 0$, and $q_P = 0$ we thus find that at $O(\epsilon)$ the semi-discrete coarse grid equations do not depend on the subgrid velocities. Consequently, the dynamics are completely described by the coarse grid balance, and the only influence of the fine grid description is that the parametrisation of the pressure curves defines the weights β assigned to the pressure gradients. To obtain the linear response, we subsequently seek for a given depth d progressive wave solutions for the coarse grid variables of the form $\hat{y}_k \exp(\mathrm{i}kx - \mathrm{i}\omega t)$, where $\hat{y}_k$ is a complex amplitude, ω is the angular frequency, and k is the wavenumber. Substitution of this ansatz, and solving the resulting equations (see Appendix B) results in an explicit expression for the coarse grid variables, the numerical dispersion relation, and derived quantities such as group velocity and wave celerity. Note that all of these depend on the order of the interpolating spline through the weights β.

In shallow water (relative depth $kd \ll 1$) the non-hydrostatic pressure approaches zero over the vertical, and expressions for the celerity and group velocity all asymptotically approach the shallow water celerity of Airy theory (Fig. 2), regardless of the order N_p. However, away from the shallow water limit the dispersive properties of the methods start to diverge from one-another, and from the Airy wave theory. For example, if we consider two coarse vertical layers, the celerity and group velocity for $kd > 1$ is generally best predicted using a linear profile and remain reasonable up to $kd \approx 5$, whereas for $kd > 2$ the other profiles – and

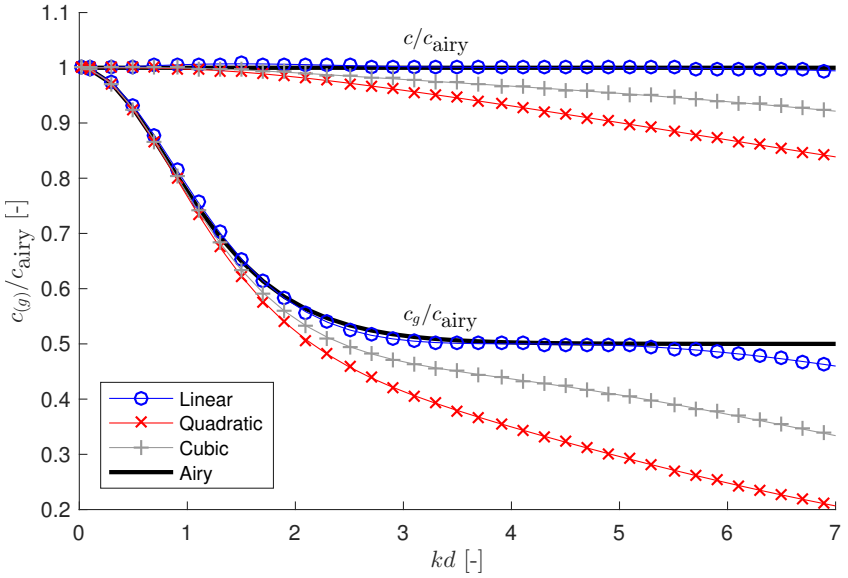

Figure 2: Dispersive properties as a function of relative depth kd for a semi discrete model with two pressure layers using linear (circle markers), quadratic (cross markers) or cubic (plus markers) splines compared with Airy linear wave theory (solid lines). The upper four curves represent the wave celerity $c = \omega/k$ whereas the lower curves depict the group velocity $c_g = \partial_k \omega$. All curves are normalised with the wave celerity from linear wave theory.

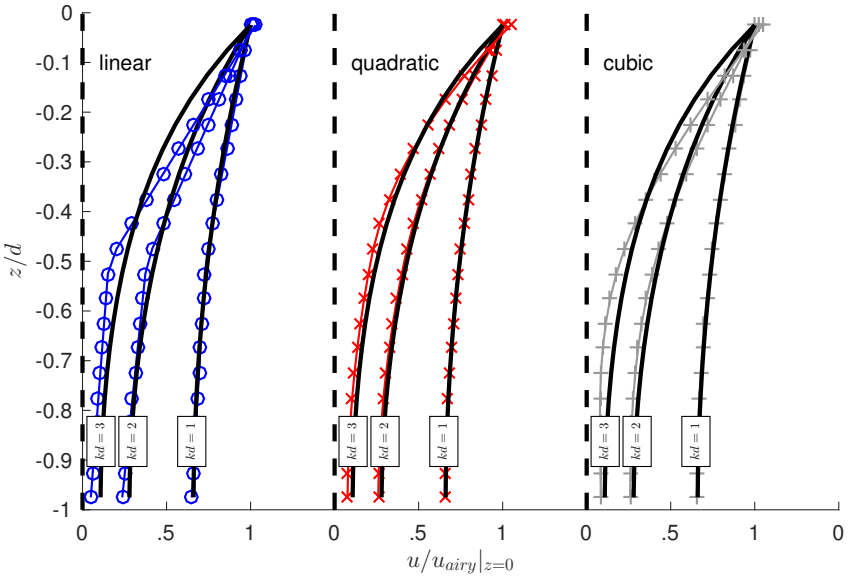

Figure 3: The horizontal velocity below the crest of a wave (scaled with the velocity at $z = 0$). Comparison between profiles obtained from Airy theory and the semi-discrete model with two pressure layers using linear (left panel), quadratic (center panel) and cubic splines (right panel). Within each panel separate curves are drawn for (from right to left) kd equals 1,2 and 3.

the quadratic splines in particular – introduce large differences. Note that with linear interpolation the dispersive properties of the subgrid method are identical to the conventional SWASH model for the same number of pressure layers, independent of the number of subgrid layers.

Inspection of the resultant velocity profiles reveals that the higher order splines do lead to qualitatively better descriptions of the vertical velocity profile (Fig. 3). The explanation that the linear method nevertheless has better dispersive properties is likely because the errors of the linear method in the lower and upper part of the water column are of opposite sign. Consequently, despite qualitatively performing worse, the errors cancel after integration, and both the net non-hydrostatic force per unit length and discharge per unit length are generally approximated better (not shown), and in fact are approximated well over a range of kd values similar to that of the wave celerity.

Although all the models improve their properties with increasing number of coarse grid layers, the choice between the interpolation techniques is a trade off between better dispersive properties over a larger range of kd values or more accurate velocity profiles at lower kd values. That said, we particularly envision the subgrid method to be used to model flows that are driven by shallow water wave processes, for which the wave induced profile does not vary strongly over the vertical, but the induced cross-shore and long-shore flows can be strongly sheared (e.g., Özkan-Haller and Kirby, 1999; MacMahan et al., 2006; Clark et al., 2012). To feasibly model these flows over domains of practical interest (say a coastal region spanning $\sim 1 \times 1$ km), we are likely restricted to a relatively small number of coarse layers ($P \sim 2$). For these applications the improved dispersive properties are useful as this allows for a correct evolution of the wave energy due to shoaling and refraction – primarily influenced by group velocity and wave celerity, respectively – whereas in shallow water ($kd < 1$), the linear representation is a reasonable approximation. These are the principal reasons that we used the subgrid method combined with linear interpolation.

4. Test cases

To validate the subgrid model, we consider three experimental test cases. The first two are the flume experiments by Ting and Kirby (1994) and Boers (1996), who made detailed measurements of the waves and mean flows for regular waves propagating over a plane beach, and irregular waves over a barred beach, respectively. The final test case considers the experiment of Visser (1991), who measured a longshore current induced by regular waves propagating over a plane beach. For fully resolved simulations (where the number of pressure layers equals the number of velocity layers), model results did not significantly improve for more than 20 pressure layers (Appendix C.1). Therefore, we take a fully resolved 20 pressure layer model as our baseline result. We compare the results of various combinations of velocity and pressure layers in the subgrid method with this baseline model, and the observations. In the following, we distinguish between these simulations according to the number of velocity and pressure layers used (e.g., 20V2P indicates a

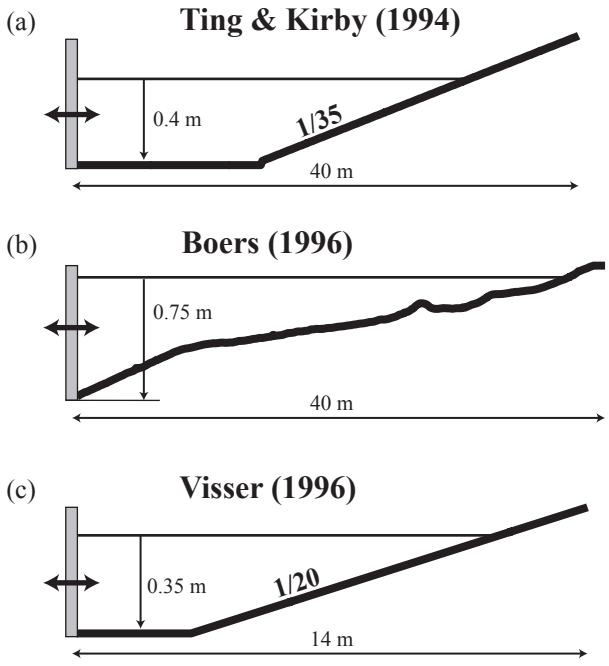

Figure 4: Experimental set-up of the three laboratory experiments.

simulation with 20 velocity layers and 2 pressure layers).

4.1. Regular waves breaking on a plane beach (Ting and Kirby, 1994)

In the experiment of Ting and Kirby (1994), cnoidal waves propagated over a 1/35 plane beach (see Fig. 4a for a sketch of the experimental layout). They considered two wave conditions with a wave height of $H = 12.5$ cm and a wave period of $T = 2$ s and 5 s, respectively. The breaking waves were of the spilling type for $T = 2$ s and of the plunging type for $T = 5$ s.

To reproduce these experiments, the model was employed with a time step of $\Delta t = 0.005s$, and a horizontal grid resolution of $\Delta x = 0.025$ m (corresponding to $O(100)$ points per wave length at the wavemaker). Following Smit et al. (2013), the numerical wavemaker was forced based on second-order cnoidal wave theory including a mass flux contribution to compensate for the non-zero mean mass influx. The roughness height was set at $d_r = 4 \times 10^{-4}$ m, a representative value for smooth concrete (e.g., Chow, 1959). Model results were analysed based on phase averaged time signals of the surface elevation, horizontal flow velocity, and turbulent kinetic energy with a length of 100 wave periods after steady state conditions were reached. To compare vertical profiles of velocity and turbulent kinetic energy, we interpolated the model predictions from the terrain-following framework to a fixed vertical grid. Variables that were located above the instantaneous free surface were set to zero. Subsequently, the mean velocities were computed at each cross-shore position by time-averaging the vertically interpolated model predictions.

To test the subgrid method, we ran 6 simulations with a varying number of pressure layers (ranging $2-20$). Fig. 5 shows the cross-shore variation of the wave height H (relative to the local mean water level), and the setup $\overline{\zeta}$ for both wave conditions. For the spilling wave condition, the waves shoal up to $x \approx 8$ m, where the wave height starts to decrease as the waves are breaking (Fig. 5a). These patterns are reproduced well by the 20V20P baseline simulation, including the onset of wave breaking near $x = 8$ m and the dissipation of wave energy in the surf zone, although H is slightly over predicted for $x < 8$ m. The baseline predictions also capture the typical magnitude of $\overline{\zeta}$, although it is under predicted just seaward of the breakpoint (Fig. 5b). Here, the measured $\overline{\zeta}$ shows a sudden jump, which can possibly be attributed to measurement inaccuracies as the physical reasons for this jump are unclear (Smit et al., 2013).

To quantify the model performance, we computed a skill index following Willmott (1981),

$$\text{Skill} = 1 - \frac{\sum_{i}^{N_i} \left(Q\left(i\right) - Q_{\text{M}}\left(i\right)\right)^2}{\sum_{i}^{N_i} \left(\left|Q\left(i\right) - \overline{Q}_{\text{M}}\right| + \left|Q_{\text{M}}\left(i\right) - \overline{Q}_{\text{M}}\right|\right)^2}, \tag{22}$$

where $Q(i)$ is the predicted quantity of interest, $Q_{\text{M}}(i)$ is the measured quantity, the vertical lines indicate the absolute value (e.g., $|Q|$), and the overline indicates the mean value (e.g., $\overline{Q}_{\text{M}}$). With this skill index we quantify whether the model predictions agree with the measurements. For a skill of 1, the model and measurements are in perfect agreement, whereas a skill of 0 indicates significant discrepancies. The skill

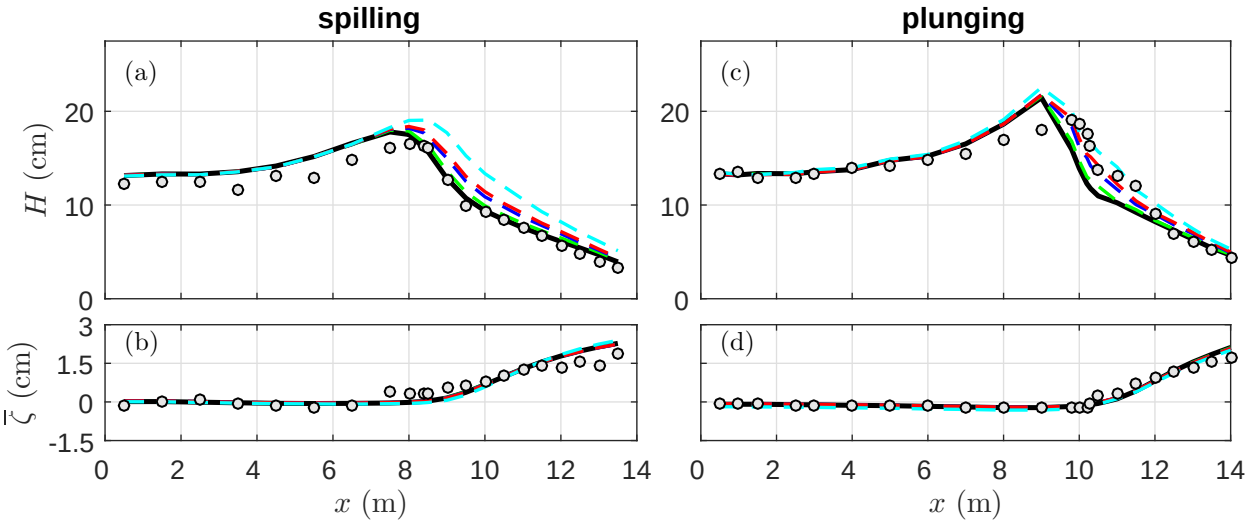

Figure 5: Comparison between predicted (lines) and measured (markers) wave parameters for the spilling (left panels) and plunging wave condition (right panels) of the Ting and Kirby (1994) experiment. The top panels, (a) and (c), show the cross-shore variation of the wave height (H) of the phase-averaged surface elevation (relative to the mean water level). The bottom panels, (b) and (d), show the cross-shore variation of the mean water level or setup ($\overline{\zeta}$). Results are given for the 20V2P (dashed cyan line), 20V4P (dashed red line), 20V5P (dashed blue line), 20V10P (dashed green line), and the 20V20P simulation (black line).

confirms that the baseline predictions of H and $\overline{\zeta}$ are in agreement with the measurements (Table 1).

Subgrid model predictions (with $2-10$ pressure layers) of the spilling wave condition are in agreement with both the measurements and the baseline simulation (Fig. 5a-b). As illustrated by the skill (Table 1), discrepancies with the measured H and $\overline{\zeta}$ typically increase for a decreasing number of pressure layers. Nonetheless, the skill of all the subgrid simulations is comparable with that of the baseline simulation. This demonstrates that the subgrid method captures the wave evolution in the surf zone with an accuracy that is comparable to the baseline model.

For the plunging breaker condition, both the subgrid model and the baseline simulation resolve the measured cross-shore variation of H and $\overline{\zeta}$ with a skill that is comparable to the results of the spilling condition (Fig. 5c-d and Table 1). All simulations over predict H just seaward of the breaking location ($x \approx 8$ m), and under predict H just shoreward of this location (except for the 20V2P simulation). This indicates that wave breaking is initiated at slightly larger water depths in the model compared to the measurements, which is consistent with the detailed non-hydrostatic simulations of Derakhti et al. (2016a).

To verify if the subgrid method can resolve the vertical dependence of the flow, Fig. 6 shows the measured and predicted vertical profiles of the (normalised) mean cross-shore velocity $\overline{u}$ and the mean turbulent kinetic energy $\overline{k_\mathrm{t}}$ at several locations near the breakpoint. For both wave conditions, the measured mean flow has a strong vertical shear as the flow is directed seaward near the bottom (commonly known as undertow) and directed shoreward near the free surface (Fig. 6a and 6c). Both the baseline simulation and the subgrid simulations reproduce the typical vertical structure of $\overline{u}$ at the various locations, including the vertical position where the flow changes direction (at $z \approx 0$ m). However, the magnitude of the flow is generally over predicted with a comparable skill for both wave conditions (Table 1). Similar to $\overline{u}$, the vertical structure of the $\overline{k}_\mathrm{t}$ predictions agrees with the measurements, although its magnitude is over predicted at the sensor locations closest to the breakpoint (Fig. 6b and 6d). Like the predictions of H, and $\overline{\zeta}$, the subgrid and baseline predictions of $\overline{u}$ and $\overline{k_\mathrm{t}}$ are of similar accuracy (Table 1). These results show that errors introduced by the subgrid method are an order of magnitude smaller compared to the differences between the measured

Table 1: Skill of the predicted bulk parameters versus the measurements for the Ting and Kirby (1994) experiment.

	Ting and Kirby (1994)									
	spilling					plunging				
	20V20P	20V10P	20V5P	20V4P	20V2P	20V20P	20V10P	20V5P	20V4P	20V2P
H	0.99	0.98	0.97	0.96	0.90	0.92	0.94	0.97	0.98	0.97
$\overline{\zeta}$	0.96	0.96	0.96	0.96	0.95	0.99	0.99	0.99	0.99	0.99
$\overline{u}$	0.84	0.85	0.86	0.86	0.87	0.83	0.84	0.84	0.84	0.85
$\overline{k}_\mathrm{t}$	0.57	0.56	0.57	0.58	0.60	0.61	0.61	0.60	0.59	0.54

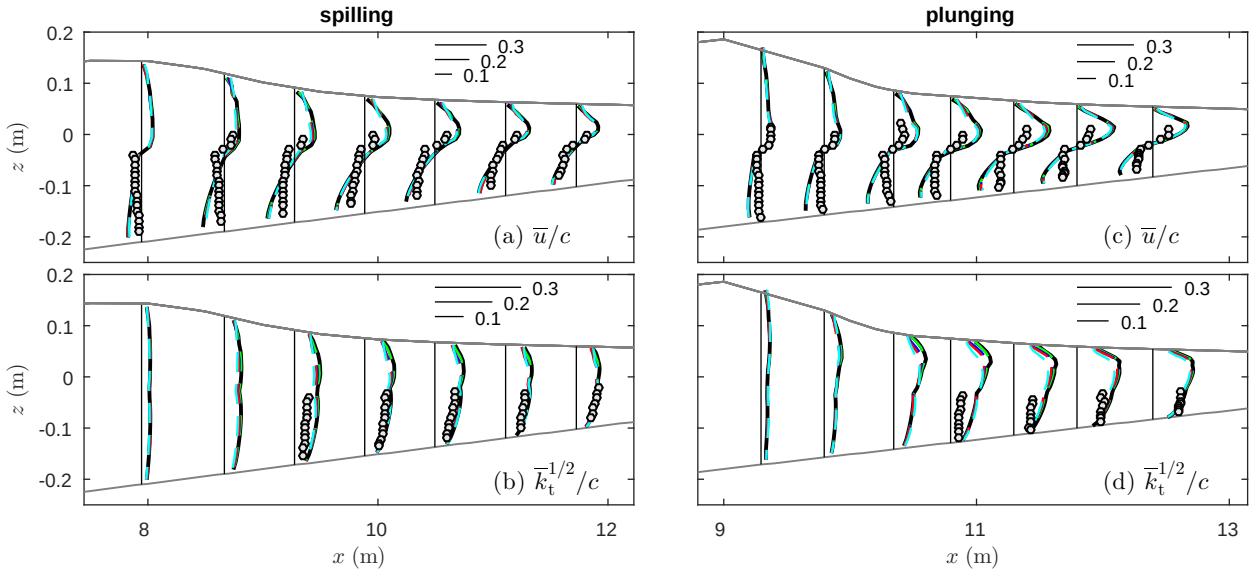

Figure 6: Comparsion between predicted (lines) and measured (markers) vertical profiles of the normalised mean cross-shore velocity $\overline{u}/c$ (top panels) and turbulent kinetic energy $\overline{k}_t^{1/2}/c$ (bottom panels) for the spilling (left panels) and plunging wave condition (right panels) of the Ting and Kirby (1994) experiment. The vertical line indicates the location and zero value for each of the vertical profiles. The horizontal oriented grey lines illustrate the wave crest level (top line) and the bottom (lower line). The horizontal lines in the top right of each panel indicates the magnitude of the respective parameter. Results are shown for the 20V2P (dashed cyan line), 20V4P (dashed red line), 20V5P (dashed blue line), 20V10P (dashed green line), and the 20V20P simulation (black line). Both the velocity and the turbulent kinetic energy are normalised with the celerity of shallow water waves $c\,(=\sqrt{gd})$.

and predicted turbulent flow field.

4.2. Random waves breaking on a barred beach (Boers, 1996)

To validate the subgrid method for spectral waves over a realistic bottom topography, we compare model results with the laboratory experiment of Boers (1996). In this experiment, the wave and velocity field of random waves propagating over a barred beach profile were measured for a total of three wave conditions (see Fig. 4b for a sketch of the experiment layout), of which we selected the conditions with the highest and lowest wave height (i.e., case B and case C, respectively). In these two experiments, waves were generated at the wavemaker based on a JONSWAP spectrum with a significant wave height of $H_{m0} = 20.6$ cm and a peak period of $T_p = 2.03$ s for case B, and $H_{m0} = 10.3$ cm and $T_p = 3.33$ s for case C.

The model was employed with a time step of $\Delta t = 0.002$ s and a horizontal grid resolution of $\Delta x = 0.02$ m. Waves were generated in accordance with Rijnsdorp et al. (2014), who used a weakly nonlinear weakly-reflective wavemaker based on measurements of the incident wave field at the first wave gauge. The roughness height and the vertical grid resolution were set in accordance with the simulations of the previous test case

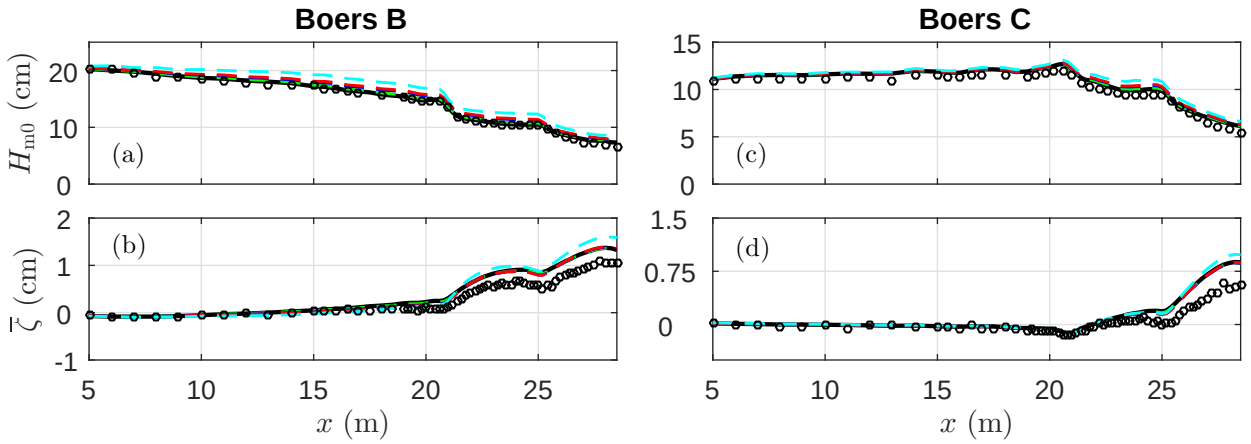

Figure 7: Comparison between predicted (lines) and measured (markers) wave parameters for the wave conditions of the Boers (1996) experiment (B: left panels, C: right panels). The top panels, (a) and (c), show the cross-shore variation of the wave height H_{m0}, and the bottom panels, (b) and (d), show the cross-shore variation of the mean water level or setup ($\overline{\zeta}$). Results are shown for the 20V4P (dashed red line), 20V5P (dashed blue line), 20V10P (dashed green line), and the 20V20P baseline simulation (black line).

(Section 4.1). Simulations had a duration of 28 min, and the measured and predicted signals were analysed after 60 s of spin-up time.

For both wave conditions, the subgrid simulations reproduced the cross-shore variation of the measured significant wave height H_{m0} (Fig. 7a and 7c), which was computed based on the variance of the surface elevation signal ($H_{m0} = 4\sqrt{\langle \zeta^2 \rangle}$, where $\langle ... \rangle$ indicates averaging in time). Furthermore, the baseline and subgrid predictions are of similar accuracy (Table 2), although errors in the subgrid predictions typically increase for a decreasing number of pressure layers P. For both wave conditions, the trend and overall magnitude of the $\overline{\zeta}$ predictions agree with the measurements, although $\overline{\zeta}$ is over predicted shoreward of $x \approx 20$ m (Fig. 7b and 7d).

As a final comparison for this flume experiment, Fig. 8 shows the vertical structure of the normalised

Table 2: Skill of the predicted bulk parameters versus the measurements for the Boers (1996) experiment.

	Boers (1996)									
	B					C				
	20V20P	20V10P	20V5P	20V4P	20V2P	20V20P	20V10P	20V5P	20V4P	20V2P
H_{m0}	1.00	1.00	0.99	0.98	0.95	0.98	0.98	0.97	0.96	0.92
$\overline{\zeta}$	0.94	0.94	0.95	0.95	0.91	0.90	0.90	0.91	0.91	0.87
$\overline{u}$	0.83	0.83	0.83	0.83	0.82	0.81	0.82	0.82	0.83	0.82
$\overline{k_t}$	0.92	0.92	0.93	0.92	0.92	0.86	0.87	0.87	0.87	0.89

$\overline{u}$ and $\overline{k}_\mathrm{t}$ at 8 positions in the surf zone for the two considered wave conditions. For both wave conditions, the $\overline{u}$ predictions show general patterns that are comparable with the measurements as the model captures the typical undertow profile in the surf zone (Fig. 8a and 8c). However, the magnitude of the mean flow is typically over predicted, and the predicted vertical variation of the flow is typically stronger compared to the measurements (e.g., $x > 23$ m for case C). For $\overline{k}_\mathrm{t}$, both its magnitude and vertical variation generally agree with the measurements (Fig. 8b and 8d). Quantitatively, Table 2 shows that the differences between the predicted and measured mean flow field $\overline{u}$ are comparable to the Ting and Kirby (1994) test case (Section 4.1, Table 1), whereas $\overline{k}_\mathrm{t}$ is predicted with better skill. Again, discrepancies between the model and the measurements are not related to the subgrid method as the accuracy of the subgrid and baseline predictions is comparable for all parameters (Table 2).

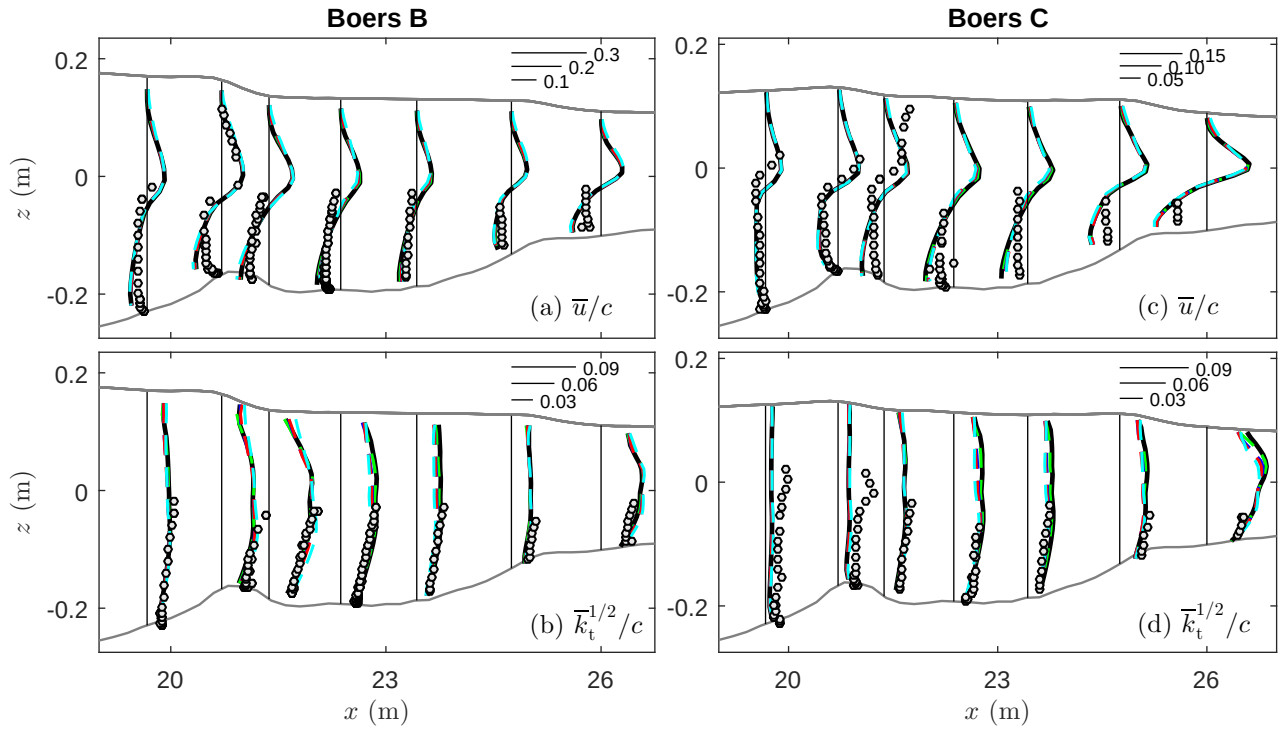

Figure 8: Comparsion between predicted (lines) and measured (markers) vertical profiles of the normalised time-averaged cross-shore velocity $\overline{u}/c$ (top panels) and turbulent kinetic energy $\overline{k}_\mathrm{t}^{1/2}/c$ (bottom panels) for the two wave conditions of Boers (1996) (B: left panels, C: right panels). The vertical line indicates the location and zero value for each of the vertical profiles. The horizontal oriented grey lines illustrate the wave height (top line) and the bottom (lower line). The horizontal lines in the top right of each panel indicates the magnitude of the respective parameter. Results are shown for the 20V4P (dashed red line), 20V5P (dashed blue line), 20V10P (dashed green line), and the 20V20P simulation (black line). Both the velocity and the turbulent kinetic energy are normalised using the celerity of shallow water waves $c\,(=\sqrt{gd})$.

4.3. Regular waves breaking on a two-dimensional plane beach (Visser, 1991)

In the final test case, model results are compared with measurements of Visser (1991), who considered the generation of a longshore current on a plane beach by the breaking of regular waves (see Fig. 4c for the cross-section of the experimental layout). Following Chen et al. (2003) and Ma et al. (2012), we consider experiment no. 4 of Visser (1991), in which a regular wave with a height of 7.8 cm and a period of 1.02 s was generated at the wavemaker with an incident angle of 15.4°.

The time step in the model simulation was set at $\Delta t = 0.005$ s, and the grid resolution was set at $\Delta x = 0.03$ m and $\Delta y = 0.044$ m (resulting in 400×128 grid cells). At the offshore boundary, waves were generated based on the target wave conditions with a weakly-reflective wavemaker based on linear wave theory. To simulate waves on an unbounded beach, a periodic boundary condition was used at the lateral boundaries of the domain. Following the previous test cases, the roughness height was set at $d_r = 4 \times 10^{-4}$ m.

The wave heights H predicted by the high-resolution simulations (with and without the subgrid method) match with the measurements throughout the domain, including the decay of the wave height as the waves start to break at $x \approx 5$ m (Fig. 9a). Furthermore, all model simulations capture the refraction of the waves

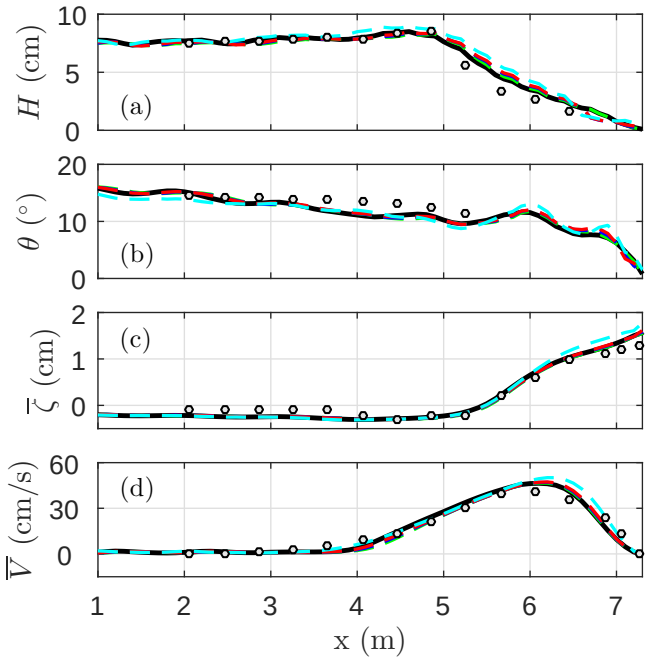

Figure 9: Comparison between predicted (lines) and measured (markers) bulk parameters for the Visser (1991) experiment. The panels show the cross-shore variation of the wave height H (a), wave direction θ (b), mean water level or setup $\overline{\zeta}$ (c), and the (depth-averaged) longshore current $\overline{V}$ (d). Results are shown for the 20V4P (dashed red line), 20V5P (dashed blue line), 20V10P (dashed green line), and the 20V20P simulation (black line).

Table 3: Skill of the predicted bulk parameters versus the measurements for the Visser (1991) experiment.

	Visser (1991)				
	20V20P	20V10P	20V5P	20V4P	20V2P
H	0.98	0.98	0.97	0.97	0.95
θ	0.73	0.73	0.73	0.75	0.69
$\overline{\zeta}$	0.98	0.98	0.98	0.98	0.96
$\overline{V}$	0.99	0.98	0.99	0.99	0.98

as they propagate shoreward, indicated by the agreement between the predicted and measured wave angle θ (Fig. 9b). In this two-dimensional domain, gradients in radiation stress due to wave breaking are balanced by a setup in $x-$direction and a longshore current in $y-$direction. For all model simulations, the typical magnitude and variation of the setup $\overline{\zeta}$ and the mean depth-averaged longshore current $\overline{V}$ agree with the measurements (Fig. 9c and Fig. 9d). The general model-data agreement observed in Fig. 9 is confirmed

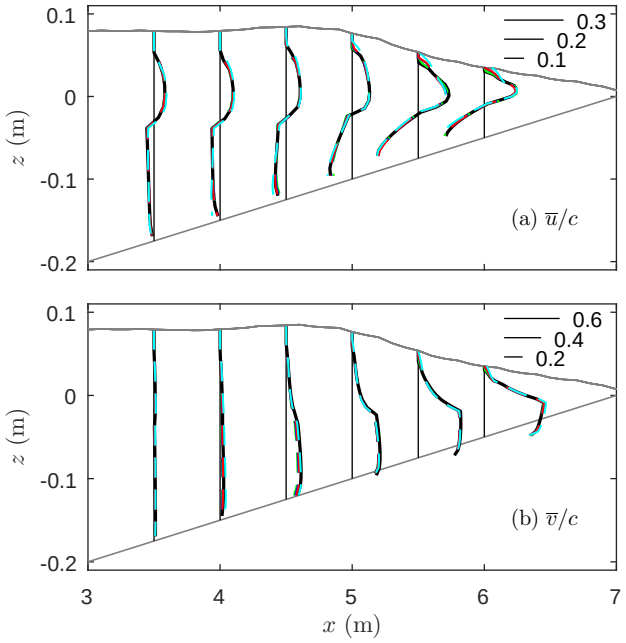

Figure 10: Predictions of the vertical profiles of the normalised time-averaged cross-shore velocity $\overline{u}/c$ (a) and alongshore velocity $\overline{v}/c$ (b) for the Visser (1991) experiment. The vertical line indicates the location and zero value for each of the vertical profiles. The horizontal oriented grey lines illustrate the wave height (top line) and the bottom (lower line). The horizontal lines in the top right of each panel indicates the magnitude of the respective parameter. Results are shown for the 20V4P (dashed red line), 20V5P (dashed blue line), 20V10P (dashed green line), and the 20V20P simulation (black line). Both the velocity and the turbulent kinetic energy are normalised using the celerity of shallow water waves $c\left(=\sqrt{gd}\right)$.

by the skill index (Table 3). Furthermore, the skill confirms that the accuracy of the subgrid and baseline predictions is comparable for all four parameters.

Unfortunately, measurements of the mean vertical flow profile are not available for this experiment. Nonetheless, to demonstrate the ability of the subgrid method in reproducing the vertical structure of the flow field, Fig. 10 shows the predicted vertical profile of the mean cross-shore $\overline{u}$ and mean alongshore velocity $\overline{v}$ at several positions near the shoreline. Similar to the previous test cases, the subgrid method reproduces the vertical $\overline{u}$ profile of the baseline predictions, including the undertow near the bed and the shoreward-directed flow in the upper part of the water column (Fig. 10a). Besides the cross-shore directed flow, the subgrid model also reproduces the vertical variation of the alongshore directed flow field $\overline{v}$ (Fig. 10b). Compared to $\overline{u}$, the alongshore directed flow field $\overline{v}$ has a weaker vertical variability in the lower part of the water column. The subgrid simulations capture these patterns, even when only a few pressure layers are used.

5. Discussion

5.1. Efficiency

The main motivation of the subgrid method is to make full 3D simulations of the wave and flow field feasible at spatial and temporal scales of a realistic field site (e.g., a domain spanning $\sim 10 \times 10$ wave lengths and a duration of $\sim$ 1000 wave periods). To quantify the efficiency gain, we consider the computational time of various simulations (including and excluding the subgrid method) with a 2V2P simulation for the

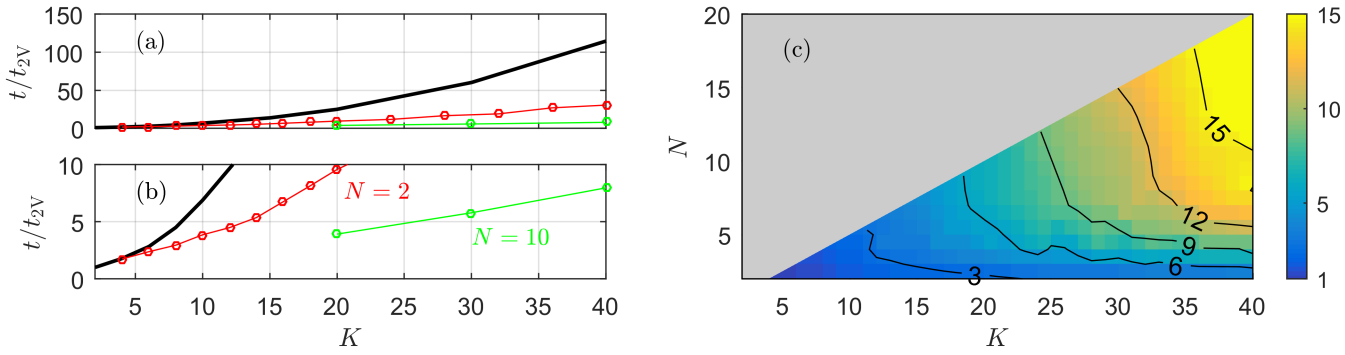

Figure 11: Panel (a): ratio of the computational time relative to a 2V2P simulation for the Visser (1991) experiment (t/t_{2V}). The ratio is depicted for non-hydrostatic simulations using the conventional model (full black line) and the subgrid approach (red and green line with circle markers). For the subgrid approach, two sets of simulations are shown with a constant number of velocity layers per pressure layer, where $N\,(= K/P)$=2 (red line) and $N = 10$ (green line), respectively. Panel (b): similar to panel (a) but with a changed vertical axis to highlight the results of the subgrid simulations. Panel (c): speed up versus a baseline simulation with the same number of velocity layers. The speed up is computed as the ratio of the computational time for a specific simulation t_i to the computational time of the corresponding baseline simulation t_b (Speed up $= t_i/t_\mathrm{b}$).

Visser (1991) experiment (Fig. 11a-b). Without the subgrid model, the computational effort increases nonlinearly when the number of layers K is increased (Fig. 11a, full black line). Such nonlinear scaling is primarily due to the increased effort required to solve the Poisson equation. When using the subgrid model, the computational effort is significantly reduced, as illustrated by the red and green line with circle markers, which correspond to simulations with two ($N = 2$) and ten velocity layers ($N = 10$) per pressure layer, respectively. For example, a 20V2P simulation takes about 4 times longer to run compared to a 2V2P simulation (Fig. 11b), whereas a 20V20P simulation takes about 25 times longer (Fig. 11a). This indicates that for this case the subgrid model is about 6 times faster than a baseline simulation with the same number of velocity layers (i.e., a speed up of 6). To further illustrate this, Fig. 11c shows the speed up of the subgrid simulations (with various N and K combinations) relative to a baseline simulation with the same number of velocity layers. The speed up of the subgrid simulations increases significantly as N and K increase. These results show that the computational effort of a high-resolution simulation can be reduced by up to an order of magnitude when using the subgrid method. Although the computational effort remains significant for such detailed simulations, the subgrid method makes them viable on state-of-the-art multi-core machines for select engineering and scientific purposes.

5.2. Accuracy

This work demonstrates that the subgrid model resolved the mean flow with an accuracy that is comparable to the fully resolved model. For the three test cases, we found that the skill (relative to the measurements) of the subgrid and baseline predictions was comparable for all considered wave and flow parameters. To analyse the accuracy of the subgrid simulations in more detail, Fig. 12 shows the root mean square error (RMSE) of the subgrid predictions with respect to a 20V20P baseline simulation. The RMSE was computed as,

$$\mathrm{RMSE} = \sqrt{\frac{1}{N_i}\sum_{i}^{N_i}\left(Q\left(i\right) - Q_{\mathrm{R}}\left(i\right)\right)^2}, \tag{23}$$

where Q_{R} is the prediction of the 20V20P baseline simulation. Compared to the baseline simulations, the RMSE of all depicted parameters decreases for a increasing number of pressure layers P, with convergence typically scaling as P^{-b} with $b \approx 0.9$ (Appendix C.2). Overall, the RMSE of the subgrid predictions are small compared to their typical measured values (e.g., the maximum RMSE of H is about 3 cm, whereas $H = \mathcal{O}\left(10\right)$ cm). Supported by the previous observations (Table 1-3), these results illustrate that the discrepancies introduced by the subgrid method are much smaller compared to the differences between the model predictions and the measurements. Even with a few pressure layers the introduction of the subgrid method does not adversely alter the accuracy of the model predictions.

These results are in accordance with our assumption that in the model equations the mean flow dynamics and wave dynamics essentially operate on two separate vertical scales, each of which can be evaluated

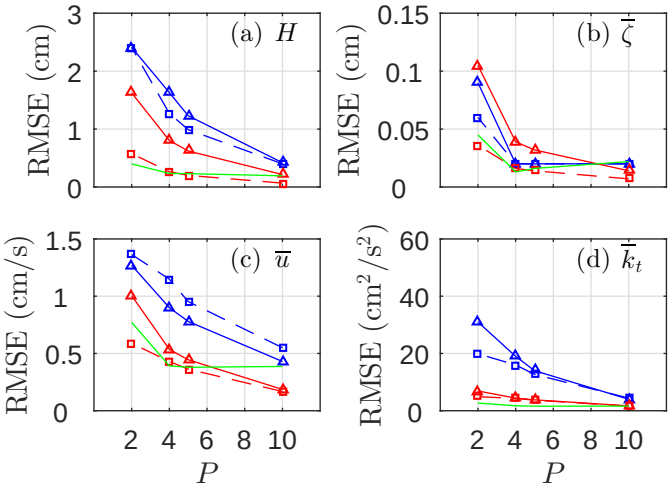

Figure 12: RMSE of all test cases relative to a 20V20P baseline simulations for the (significant) wave height H (a), mean water level $\overline{\zeta}$ (b), mean cross-shore velocity $\overline{u}$ (c), and mean turbulent kinetic energy $\overline{k}_\mathrm{t}$ (d). The colors indicate the test case; where blue corresponds to Ting and Kirby (1994), red to Boers (1996), and green to Visser (1991). For the first two test cases, the full line with triangular markers and the dashed line with square markers corresponds to the experiment with the largest and smallest wave height, respectively.

on separate grids. Arguably, the agreement between the fully resolved model and the subgrid model is sufficient to highlight this, whereas the comparison with observations mostly highlights deficiencies that are also present in the fully resolved model. We stress that, in the present form, predictions of the mean flow dynamics are more than reasonable, but acknowledge that discrepancies between the measured and predicted flow field can be found. These are typically largest in the surf zone, near the bed, and in the upper part of the water column. They can presumably (at least in part) be attributed to deficiencies in the turbulent closure approximations; such as the omission of wave breaking-generated turbulence at the free surface, and an incomplete description of the bottom boundary layer. Furthermore, flow predictions in the surf zone are sensitive to the specific closure model (Brown et al., 2016), and the standard $k-\epsilon$ model adopted here may not be the most suitable closure model in this highly dynamic region. Regardless, these deficiencies are not specific to the subgrid method presented here, but are inherited from the fully resolved model, and thus do not invalidate the subgrid approach.

5.3. Wave breaking

As the waves approach the shore, waves start to steepen and strong vertical gradients in the horizontal particle velocities develop (with larger velocities near the surface compared to the bottom), and they eventually break when the wave shape becomes unstable. Neither the subgrid model nor the fully resolved model contain any parameters that control the onset or cessation of this wave breaking, or the dissipation rate. As

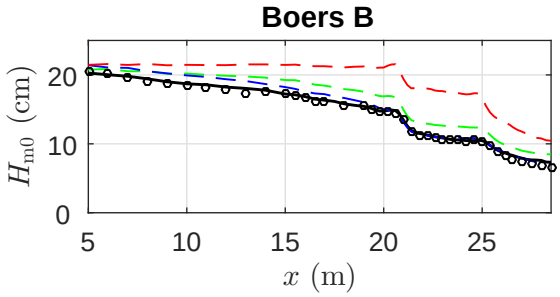

Figure 13: Comparison between predicted (lines) and measured (markers) wave heights H_{m0} for the case B of the Boers (1996) experiment. Results are shown for the 20V2P (dashed green line), 2V2P without HFA (dashed red line), 2V2P with HFA (dashed blue line), and 20V20P baseline simulation (black line).

long as the model properly conserves momentum over flow discontinuities, both the transition of a wave into a bore and its dissipation rate follow naturally. In the context of the SWASH model this was established previously by Smit et al. (2013). However, they also found that incipient breaking in SWASH is delayed considerably if a low vertical resolution is used. Their hypothesis for this delayed transition (confirmed with numerical simulations) was that at low vertical resolutions the horizontal velocities near the surface are underestimated, so that the kinematic conditions for the onset of breaking (i.e., particle velocities larger than the wave celerity) are shifted shoreward (Refer to Smit et al., 2013, for more details). For that reason, SWASH simulations with low vertical resolutions (e.g., a 2V2P simulations) typically employ a heuristic approximation (referred to as the hydrostatic front approximation, or HFA) to ensure that wave breaking occurs at the correct location.

The subgrid methodology introduced in the present work was primarily intended to resolve the vertical variations in the mean flow. Effectively, all terms except for the vertical accelerations and non-hydrostatic pressure gradients are resolved on the fine grid, including the horizontal advection terms. The enhanced velocities near the surface due to wave non-linearity appear to be well resolved in a subgrid model with 20 velocity layers, regardless of the number of pressure points, as the location of incipient breaking is well approximated. For instance, if we consider case B of the Boers (1996) experiment, and compare a 2V2P model (with and without HFA) to the subgrid simulations, we see that the 20V2P subgrid model predicts the reduction in wave height much better than the 2V2P without HFA (Fig. 13, dashed green versus dashed red line). In fact, the predictions of the 20V2P subgrid model are comparable to the 20V20P baseline model, and the 2V2P model with HFA enabled. However, if one is solely interested in the wave dynamics, the subgrid method is not directly competitive with a 2V2P model with HFA in terms of computational efficiency, as the subgrid method still requires a high number of velocity layers. Nonetheless, these results are encouraging as they imply that for typical coastal applications the subgrid method requires no empirically based approximation to account for the wave-breaking induced bulk dissipation of the wave motion.

6. Conclusions

In this work, we have presented a subgrid approach for the wave-resolving non-hydrostatic modelling framework that aims to efficiently simulate the vertical structure of wave-induced currents in coastal regions. With this approach, the wave and mean flow dynamics are essentially solved on different grids: a coarse grid for the vertical accelerations and pressure gradients, and a fine (or sub-) grid to resolve the horizontal accelerations and stress divergence. The principal advantage of this approach is that the effort required to solve the pressures through the Poisson equation can be reduced by an order of magnitude. We implemented the subgrid approach in the open-source non-hydrostatic wave-flow model SWASH, and validated the resulting model for the wave and current field using a total of three test cases that comprise a range of wave conditions (including regular waves on a plane beach and random waves on a realistic bottom topography). Subgrid predictions were compared to the measurements, and to a high-resolution fully resolved SWASH simulation (with an equal number of coarse and fine grid layers)

For all considered test cases, the subgrid simulations captured the measured cross-shore variation of the wave field with an accuracy that is comparable to the fully resolved SWASH simulations. This includes the initiation of wave breaking and the bulk dissipation of wave energy in the surf zone. The subgrid method resolved the cross-shore evolution of the bulk wave parameters with as few as two pressure layers. Remarkably, the subgrid method required no additional measures to initiate wave breaking, in contrast with conventional SWASH simulations that employ a coarse vertical resolution (e.g., Smit et al., 2013).

Discrepancies between the predicted and measured turbulent flow field were typically an order of magnitude larger compared to the wave field. Despite these differences, the model reproduced the typical vertical structure of the mean flow, including the undertow near the bottom and the shoreward-directed flow near the free surface. More importantly, the subgrid and fully resolved predictions were of similar accuracy, which demonstrates that the model accuracy was not significantly influenced by the introduction of the subgrid method. We anticipate that model predictions can be improved by adopting a different turbulence closure model (e.g., the nonlinear instead of the standard $k-\epsilon$ model), by including (a parametrisation of) the wave-breaking induced turbulence at the free surface, and by improving the modelling of the bottom-boundary layer.

Overall, the results of this study have shown that the introduction of the subgrid method in SWASH allows us to efficiently resolve the wave and flow field in the coastal region with an accuracy that is comparable to the fully resolved SWASH model. The primary advantage of the subgrid method is its gain in efficiency when resolving the three-dimensional flow field, which makes high resolution model applications viable at intermediate spatial and temporal scales.

Acknowledgements

This research was made possible by a grant from The Gulf of Mexico Research Initiative, and supported by resources provided by the Pawsey Supercomputing Centre with funding from the Australian Government and the Government of Western Australia.

Appendix A. Turbulent stress approximations

The turbulent stresses $\tau_{\alpha\beta}$ are approximated from the eddy viscosity approximations,

$$\begin{aligned} \tau_{xx} &= \nu \frac{\partial u}{\partial x}, \quad \tau_{xy} = \tau_{yx} = \frac{\nu}{2}\left(\frac{\partial v}{\partial x} + \frac{\partial u}{\partial y}\right), \\ \tau_{yy} &= \nu \frac{\partial v}{\partial y}, \quad \tau_{yz} = \tau_{zy} = \frac{\nu}{2}\left(\frac{\partial v}{\partial z} + \frac{\partial w}{\partial y}\right), \\ \tau_{zz} &= \nu \frac{\partial w}{\partial z} \quad \tau_{zx} = \tau_{xz} = \frac{\nu}{2}\left(\frac{\partial u}{\partial z} + \frac{\partial w}{\partial x}\right), \end{aligned} \tag{A.1}$$

where ν is the eddy viscosity estimate from a closure approximation. In 3D wave-averaged circulation models, the vertical and horizontal gradients of the vertical velocity are typically neglected. Furthermore, separate eddy viscosities are commonly introduced for the horizontal and vertical mixing (i.e., ν_h and ν_v, respectively) to account for the differences between the resolutions of the horizontal and vertical scale. In this case, the stress terms can be approximated as

$$\tau_{xx} = \nu_h \frac{\partial u}{\partial x}, \quad \tau_{yy} = \nu_h \frac{\partial v}{\partial y}, \quad \tau_{zz} = 0, \quad \tau_{xy} = \tau_{yx} = \frac{\nu}{2}\left(\frac{\partial v}{\partial x} + \frac{\partial u}{\partial y}\right), \quad \tau_{yz} = \tau_{zy} = \nu_v \frac{\partial v}{\partial z}, \quad \tau_{zx} = \tau_{xz} = \nu_v \frac{\partial u}{\partial z}. \tag{A.2}$$

A more complete description of the turbulent stresses in the surf zone requires to account the wave breaking generated turbulence, which is beyond the scope of the present work. For that reason we have opted to retain the approximate relations coupled to a $k - \epsilon$ model (Launder and Spalding, 1974) to estimate the vertical eddy viscosity ν_v, and Smagorinsky-type approximation (Smagorinsky, 1963) to estimate the horizontal eddy viscosity ν_h. Note that a more complete description may improve the inter-comparison between model results and observations, but the relative performance between a subgrid and fully resolved model is likely unaffected.

Appendix B. Linear Semi-Discrete Analysis

To determine the linear response of the system for different parametrisations of the pressure curve we express the semi-discrete linear system for constant depth in matrix vector form,

$$\mathbf{A}_{\partial_t, \partial_x} \boldsymbol{y} = 0, \tag{B.1}$$

where $\boldsymbol{y}^T = [\zeta, U_1, \ldots, U_P, W_0, \ldots, W_{P-1}, q_1, \ldots, q_P]$ is the solution vector of the coarse grid variables, and

$$\mathbf{A}_{\partial_t,\partial_x} = \begin{bmatrix} \partial_t & [0,\ldots,0] & [1,0,\ldots,0] & [0,\ldots,0] \\ g\begin{bmatrix}1\\ \vdots \\ 1\end{bmatrix}\partial_x & \mathbf{I}\partial_t & \mathbf{0} & H^{-1}\boldsymbol{P}\partial_x \\ \begin{bmatrix}0\\ \vdots \\ 0\end{bmatrix} & \mathbf{0} & \frac{1}{2}(\mathbf{I}+\mathbf{D}^+)\partial_t & -(\mathbf{I}-\mathbf{D}^-)H^{-1} \\ \begin{bmatrix}0\\ \vdots \\ 0\end{bmatrix} & \mathbf{I}\partial_x & (\mathbf{I}-\mathbf{D}^+)H^{-1} & \mathbf{0} \end{bmatrix}, \tag{B.2}$$

is the $3P+1$ by $3P+1$ matrix that represents the dynamics of the semi-discrete system; and which from top to bottom consists of semi-discrete representations of the kinematic surface boundary condition, the horizontal momentum balance, the vertical momentum balance, and local continuity. Here $\mathbf{I}$ and $\mathbf{0}$ are the P by P identity and zero matrices, respectively, and $D^{\pm}_{i,j} = \delta_{i,j\pm1}$ denotes a matrix where the upper (+) or lower (-) off-diagonal is unity. Finally,

$$\mathrm{P_{i,j}} = \sum_{n=0}^{N_p} \frac{\beta_{n,i,j}}{n+1} H_i^{n+1}, \tag{B.3}$$

represents the influence of the layer integrated pressure curve.

To analyze the linear response for a progressive wave, we substitute the ansatz,

$$\boldsymbol{y} = \hat{\boldsymbol{y}} \exp(\mathrm{i}kx - \mathrm{i}\omega t), \tag{B.4}$$

where $\hat{y}^T = [\hat{\zeta}, \hat{U}_1, \ldots, \hat{U}_P, \hat{W}_1, \ldots, \hat{W}_{P-1}, \hat{q}_1, \ldots, \hat{q}_P]$ denotes the vector of complex amplitudes. Consequently, for wave like solutions $\hat{\boldsymbol{y}}$ we have $\mathbf{A}_{-\mathrm{i}\omega,\mathrm{i}k}\hat{\boldsymbol{y}} = 0$, and for non-trivial solutions to exist we demand that the matrix is singular, that is, $\mathrm{Det}(\mathbf{A}_{-\mathrm{i}\omega,\mathrm{i}k}) = 0$. This gives a condition that implies that the wavenumber and angular frequency are related, which when solving for ω gives the numerical dispersion relation $\omega = \omega(k)$. To determine $\hat{\boldsymbol{y}}$ we substitute the dispersion relation, and parametrise the nullspace of $\mathrm{A}_{-\mathrm{i}\omega(k),\mathrm{i}k}$ in terms of the free surface amplitude.

Appendix C. Convergence

Appendix C.1. Baseline model

To decide on the number of velocity layers to be used in this paper, we tested the convergence behaviour of the model for an increasing vertical grid resolution (without using the subgrid method). For this purpose, a series of simulations was conducted for the spilling wave condition of the Ting and Kirby (1994) experiment with a varying number of vertical layers ($K = 10 - 40$). To test the convergence behaviour of the model, we computed the RMSE for the wave height (H) and the mean cross-shore velocity ($\overline{u}$) at all experimental

sensor locations. As expected, the RMSE of both variables reduces for an increasing number of vertical layers (Fig. C.1). In general, differences with the baseline simulation are largest for $\overline{u}$. For both parameters, the convergence rate is approximately 1.5. For $K \geq 20$ layers the wave and flow parameters were predicted with small errors compared to the 40 layer simulation. Based on these findings, we used 20 velocity layers in the simulations of this work.

Appendix C.2. Subgrid model

The convergence behaviour of numerical models generally depends on the accuracy of the numerical schemes used in the model. For example, when second-order schemes are used for the spatial derivatives, the model results are expected to converge quadratically when the grid resolution is refined. However, due the the use of a coarse and fine grid to resolve the various variables, the convergence rate of the subgrid model is not obvious. For that reason, we conducted a convergence test for the spilling wave condition of the Ting and Kirby (1994) experiment. We considered a series of simulations with an increasing number of pressure layers ($P = 2 - 10$), and with a constant number of 20 velocity layers. To quantify the convergence of the subgrid method, we computed the RMSE for two parameters (H, and $\overline{u}$) relative to a 20V20P reference simulation. Convergence is approximately linear for both parameters, although it is slightly better for the wave heights H than for the mean cross-shore flow (Fig. C.2).

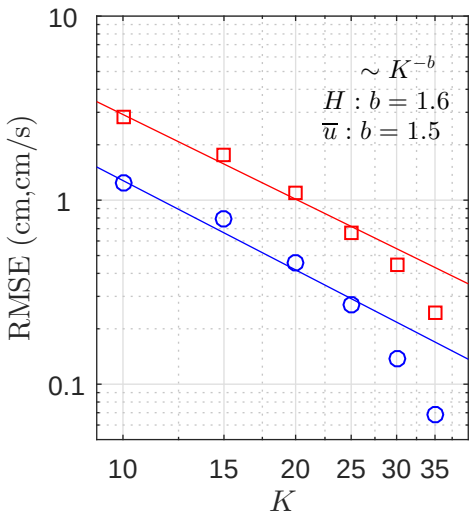

Figure C.1: RMSE of the wave height H (blue line with circle markers), and time-averaged cross-shore velocity $\overline{u}$ (red line with square markers) for a varying number of vertical layers K versus a 40V40P reference simulation. The markers indicate the computed SI, and the line indicates the best fit for a K^{-b} power function. For all three parameters, the coefficient b is depicted in the top right corner of both panels.

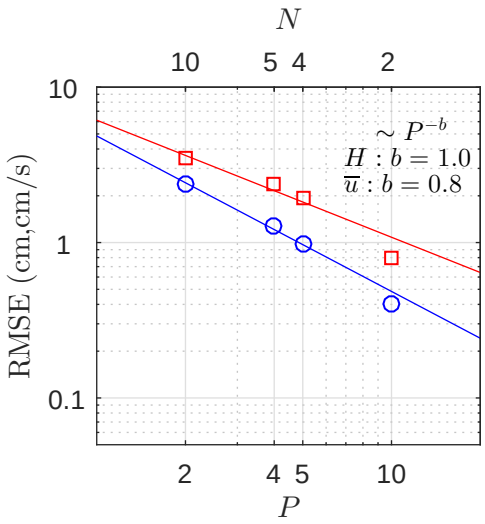

Figure C.2: RMSE of the wave height H (blue line with circle markers), and time-averaged cross-shore velocity $\overline{u}$ (red line and square markers) for a varying number of pressure layers P with a constant number of 20 velocity layers versus a 20V20P baseline simulation. The markers indicate the computed error, and the line indicates the best fit for a P^{-b} power function. For all three parameters, the coefficient b is depicted in the top right corner of both panels. The top axis indicate the number of velocity layers per pressure layer $N(= {}^{K}/_{P})$.

References

Andrews, D.G., Mcintyre, M.E., 1978. An exact theory of nonlinear waves on a Lagrangian-mean flow. Journal of Fluid Mechanics 89, 609.

Bai, Y., Cheung, K.F., 2013. Dispersion and nonlinearity of multi-layer non-hydrostatic free-surface flow. Journal of Fluid Mechanics 726, 226–260.

Boers, M., 1996. Simulation of a surf zone with a barred beach; report 1: Wave heights and wave breaking. Technical Report. Delft University of Technology.

Bonneton, P., Barthelemy, E., Chazel, F., Cienfuegos, R., Lannes, D., Marche, F., Tissier, M., 2011. Recent advances in Serre-Green Naghdi modelling for wave transformation, breaking and runup processes. European Journal of Mechanics - B/Fluids 30, 589–597.

Bradford, S.F., 2011. Nonhydrostatic Model for Surf Zone Simulation. Journal of Waterway, Port, Coastal, and Ocean Engineering 137, 163–174.

Bradford, S.F., 2014. Vertical grid design for more accurate and efficient surf zone simulation. Coastal Engineering Journal 56.

Brown, S.A., Greaves, D.M., Magar, V., Conley, D.C., 2016. Evaluation of turbulence closure models under spilling and plunging breakers in the surf zone. Coastal Engineering 114, 177–193.

Buckley, M., Lowe, R., Hansen, J., 2014. Evaluation of nearshore wave models in steep reef environments. Ocean Dynamics 64, 847–862.

Chen, Q., Kirby, J.T., Dalrymple, R.A., Shi, F., Thornton, E.B., 2003. Boussinesq modeling of longshore currents. Journal of Geophysical Research 108.

Chow, V.T., 1959. Open-channel hydraulics. McGraw-Hill.

Clark, D.B., Elgar, S., Raubenheimer, B., 2012. Vorticity generation by short-crested wave breaking. Geophysical Research Letters 39.

683 Craik, A.D.D., Leibovich, S., 1976. A rational model for Langmuir circulations. J. Fluid Mech 73, 401–426.
684 Cui, H., Pietrzak, J.D., Stelling, G.S., 2012. Improved efficiency of a non-hydrostatic, unstructured grid, finite volume model.
685 Ocean Modelling 54-55, 55–67.
686 Dalrymple, R.A., MacMahan, J.H., Reniers, A.J.H.M., Nelko, V., 2011. Rip Currents. Annual Review of Fluid Mechanics 43,
687 551–581.
688 De Bakker, A.T.M., Tissier, M.F.S., Ruessink, B.G., 2016. Beach steepness effects on nonlinear infragravity-wave interactions:
689 A numerical study. Journal of Geophysical Research: Oceans 121, 554–570.
690 Derakhti, M., Kirby, J.T., Shi, F., Ma, G., 2016a. Wave breaking in the surf zone and deep-water in a non-hydrostatic RANS
691 model. Part 1: Organized wave motions. Ocean Modelling .
692 Derakhti, M., Kirby, J.T., Shi, F., Ma, G., 2016b. Wave breaking in the surf zone and deep water in a non-hydrostatic RANS
693 model. Part 2: Turbulence and mean circulation. Ocean Modelling .
694 Feddersen, F., Guza, R.T., 2003. Observations of nearshore circulation: Alongshore uniformity. Journal of Geophysical Research
695 108, 3006.
696 Gomes, E.R., Mulligan, R.P., Brodie, K.L., McNinch, J.E., 2016. Bathymetric control on the spatial distribution of wave
697 breaking in the surf zone of a natural beach. Coastal Engineering 116, 180–194.
698 Groeneweg, J., Klopman, G., 1998. Changes of the mean velocity profiles in the combined wavecurrent motion described in a
699 GLM formulation. Journal of Fluid Mechanics 370, S0022112098002018.
700 Haller, M.C., Dalrymple, R.A., Svendsen, I.A., 2002. Experimental study of nearshore dynamics on a barred beach with rip
701 channels. Journal of Geophysical Research 107, 3061.
702 Hansen, 1956. Theorie zur Errechnung des Wasserstandes und der Strömingen in Randmeeren nebst Anwendungen. Tellus 8,
703 289–300.
704 van Kan, J., 1986. A Second-Order Accurate Pressure-Correction Scheme for Viscous Incompressible Flow. SIAM Journal on
705 Scientific and Statistical Computing 7, 870–891.
706 Kennedy, A.B., Chen, Q., Kirby, J.T., Dalrymple, R.A., 2000. Boussinesq Modeling of Wave Transformation, Breaking, and
707 Runup. I: 1D. Journal of Waterway, Port, Coastal, and Ocean Engineering 126, 39–47.
708 Kennedy, A.B., Thomas, D., 2004. Drifter measurements in a laboratory rip current. Journal of Geophysical Research: Oceans
709 109.
710 Kumar, N., Voulgaris, G., Warner, J.C., Olabarrieta, M., 2012. Implementation of the vortex force formalism in the coupled
711 ocean-atmosphere-wave-sediment transport (COAWST) modeling system for inner shelf and surf zone applications. Ocean
712 Modelling 47, 65–95.
713 Launder, B.E., Spalding, D.B., 1974. The numerical computation of turbulent flows. Computer Methods in Applied Mechanics
714 and Engineering 3, 269–289.
715 Lin, P., Liu, P.L.F., 1998. A numerical study of breaking waves in the surf zone. Journal of Fluid Mechanics 359, 239–264.
716 Longuet-Higgins, M.S., Stewart, R.W., 1962. Radiation stress and mass transport in gravity waves, with application to surf
717 beats'. Journal of Fluid Mechanics 13, 481–504.
718 Longuet-Higgins, M.S., Stewart, R.W., 1964. Radiation stresses in water waves; a physical discussion, with applications. Deep
719 Sea Research 11, 529–562.
720 Ma, G., Shi, F., Kirby, J.T., 2012. Shock-capturing non-hydrostatic model for fully dispersive surface wave processes. Ocean
721 Modelling 43-44, 22–35.
722 MacMahan, J.H., Reniers, A.J.H.M., Thornton, E.B., Stanton, T.P., 2004. Surf zone eddies coupled with rip current morphol-
723 ogy. Journal of Geophysical Research: Oceans 109.
724 MacMahan, J.H., Thornton, E.B., Reniers, A.J.H.M., 2006. Rip current review. Coastal Engineering 53, 191–208.
725 MacMahan, J.H., Thornton, E.B., Stanton, T.P., Reniers, A.J.H.M., 2005. RIPEX: Observations of a rip current system.

Marine Geology 218, 113–134.

Madsen, P.A., Murray, R., Sørensen, O.R., 1991. A new form of the Boussinesq equations with improved linear dispersion characteristics. Coastal Engineering 15, 371–388.

McCarroll, R.J., Castelle, B., Brander, R.W., Scott, T., 2015. Modelling rip current flow and bather escape strategies across a transverse bar and rip channel morphology. Geomorphology 246, 502–518.

McWilliams, J.C., Restrepo, J.M., Lane, E.M., 2004. An asymptotic theory for the interaction of waves and currents in coastal waters. Journal of Fluid Mechanics 511, 135–178.

Mellor, G., 2016. On theories dealing with the interaction of surface waves and ocean circulation. Journal of Geophysical Research: Oceans 121, 4474–4486.

Nicolae Lerma, A., Pedreros, R., Robinet, A., Sénéchal, N., 2017. Simulating wave setup and runup during storm conditions on a complex barred beach. Coastal Engineering 123, 29–41.

Özkan-Haller, H.T., Kirby, J.T., 1999. Nonlinear evolution of shear instabilities of the longshore current: A comparison of observations and computations. Journal of Geophysical Research 104, 25953–25984.

Reniers, A.J.H.M., Battjes, J.A., 1997. A laboratory study of longshore currents over barred and non-barred beaches. Coastal Engineering 30, 1–21.

Reniers, A.J.H.M., MacMahan, J.H., Thornton, E.B., Stanton, T.P., Henriquez, M., Brown, J.W., Brown, J.A., Gallagher, E., 2009. Surf zone surface retention on a rip-channeled beach. Journal of Geophysical Research 114, C10010.

Rijnsdorp, D.P., Ruessink, G., Zijlema, M., 2015. Infragravity-wave dynamics in a barred coastal region, a numerical study. Journal of Geophysical Research: Oceans 120, 4068–4089.

Rijnsdorp, D.P., Smit, P.B., Zijlema, M., 2014. Non-hydrostatic modelling of infragravity waves under laboratory conditions. Coastal Engineering 85, 30–42.

Ruessink, B.G., Miles, J.R., Feddersen, F., Guza, R.T., Elgar, S., 2001. Modeling the alongshore current on barred beaches. Journal of Geophysical Research: Oceans 106, 22451–22463.

Ruju, A., Lara, J.L., Losada, I.J., 2014. Numerical analysis of run-up oscillations under dissipative conditions. Coastal Engineering 86, 45–56.

Shi, J., Shi, F., Kirby, J.T., Ma, G., Wu, G., Tong, C., Zheng, J., 2015. Pressure Decimation and Interpolation (PDI) method for a baroclinic non-hydrostatic model. Ocean Modelling 96, 265–279.

Smagorinsky, J., 1963. General circulation experiments with the primitive equations. Monthly Weather Review 91, 99–164.

Smit, P., Janssen, T., Holthuijsen, L., Smith, J., 2014. Non-hydrostatic modeling of surf zone wave dynamics. Coastal Engineering 83, 36–48.

Smit, P., Zijlema, M., Stelling, G., 2013. Depth-induced wave breaking in a non-hydrostatic, near-shore wave model. Coastal Engineering 76, 1–16.

Stelling, G., Zijlema, M., 2003. An accurate and efficient finite-difference algorithm for non-hydrostatic free-surface flow with application to wave propagation. International Journal for Numerical Methods in Fluids 43, 1–23.

Stelling, G.S., Duinmeijer, S.P.A., 2003. A staggered conservative scheme for every Froude number in rapidly varied shallow water flows. International Journal for Numerical Methods in Fluids 43, 1329–1354.

Ting, F.C.K., Kirby, J.T., 1994. Observation of undertow and turbulence in a laboratory surf zone. Coastal Engineering 24, 51–80.

Tissier, M., Bonneton, P., Marche, F., Chazel, F., Lannes, D., 2012. A new approach to handle wave breaking in fully non-linear Boussinesq models. Coastal Engineering 67, 54–66.

Uchiyama, Y., McWilliams, J.C., Shchepetkin, A.F., 2010. Wavecurrent interaction in an oceanic circulation model with a vortex-force formalism: Application to the surf zone. Ocean Modelling 34, 16–35.

Van Reeuwijk, M., 2002. Efficient simulation of non-hydrostatic free-surface flow. Msc thesis. Delft University of Technology.

769 Visser, P.J., 1991. Laboratory measurements of uniform longshore currents. Coastal Engineering 15, 563–593.
770 Wei, G., Kirby, J.T., Grilli, S.T., Subramanya, R., 1995. A fully nonlinear Boussinesq model for surface waves. Part 1. Highly
771 nonlinear unsteady waves. Journal of Fluid Mechanics 294, 71.
772 Willmott, C.J., 1981. On the validation of models. Physical Geography 2, 184–194.
773 Yamazaki, Y., Kowalik, Z., Cheung, K.F., 2009. Depth-integrated, non-hydrostatic model for wave breaking and run-up.
774 International Journal for Numerical Methods in Fluids 61, 473–497.
775 Zijlema, M., Stelling, G., Smit, P., 2011. SWASH: An operational public domain code for simulating wave fields and rapidly
776 varied flows in coastal waters. Coastal Engineering 58, 992–1012.
777 Zijlema, M., Stelling, G.S., 2005. Further experiences with computing non-hydrostatic free-surface flows involving water waves.
778 International Journal for Numerical Methods in Fluids 48, 169–197.
779 Zijlema, M., Stelling, G.S., 2008. Efficient computation of surf zone waves using the nonlinear shallow water equations with
780 non-hydrostatic pressure. Coastal Engineering 55, 780–790.